Three-Dimensional Unstructured Gridding for Complex Wells and Geological Features in Subsurface Reservoirs, with CVD-MPFA Discretization Performance

Shahid Manzoor, Michael G. Edwards[1], Ali H. Dogru

Abstract

Grid generation for reservoir simulation, must honour classical key geological features and multilateral wells. The features to be honored are classified into two groups; 1) involving layers, faults, pinchouts and fractures, and 2) involving well distributions. In the former, control-volume boundary aligned grids (BAGs) are required, while in the latter, control-point (defined as the centroid of the control-volume) well aligned grids (WAGs) are required. Depending on discretization method type and formulation, a choice of control-point and control-volume type is made, i.e. for a cell-centred method the primal grid cells act as control-volumes, otherwise for a vertex-centred method the dual-grid cells act as control-volumes. Novel three-dimensional unstructured grid generation methods are proposed that automate control-volume boundary alignment to geological features and control point alignment to complex wells, yielding essentially perpendicular bisector (PEBI) meshes either with respect to primal or dual-cells depending on grid type. Both grid types use tetrahedra, pyramids, prisms and hexahedra as grid elements. Primal-cell feature aligned grids are generated using special boundary surface protection techniques together with constrained cell-centred well trajectory alignment. Dual-cell feature aligned grids are generated from underlying primal-meshes, whereby features are protected such that dual-cell control-volume faces are aligned with interior feature boundaries, together with protected vertex-centred (control point) well trajectory alignment.

[1]Swansea University

The novel methods of grid generation presented enable practical application of both method types in 3-D for the first time. The primal and dual grids generated here demonstrate the gridding methods, and enable the first comparative performance study of cell-vertex versus cell-centered control-volume distributed multi-point flux approximation (CVD-MPFA) finite-volume formulations using equivalent mesh resolution on challenging problems in 3-D. Pressure fields computed by the cell-centered and vertex-centered CVD-MPFA schemes are compared and contrasted relative to the respective degrees of freedom employed, and demonstrate the relative benefits of each approximation type. Stability limits of the methods are also explored. For a given mesh the cell-vertex method uses approximately a fifth of the unknowns used by a cell-centered method and proves to be the most beneficial with respect to accuracy and efficiency. Numerical results show that vertex-centered CVD-MPFA methods outperform cell-centered CVD-MPFA method.

Keywords: Boundary aligned unstructured hybrid gridding; Three dimensional Delaunay mesh generation; Control Volume Distributed Multipoint Flux Approximation (CVD-MPFA); Cell-centered versus vertex-centered methods;

1. Introduction

General reservoir geometries are comprised of various features such as faults, fractures, pinch-outs and layered media, with a wide range of variations in porosity and permeability across different layers, e.g., [80, 54, 55, 56, 41, 5, 43, 75, 76, 9] where a range of gridding strategies are presented. In addition reservoirs can have a complex spatial distribution of wells in place [5, 28]. In order to minimize the effects of grid orientation and discretization errors in simulation of hydrocarbon flows, grids generated should conform as closely as possible to geological features, while maintaining compatibility with the flux approximation schemes employed.

In three dimensions the term primal-cell grid is used for meshes comprised

of tetrahedra, pyramids, prisms, and/or hexahedra cells. Whereas, a dual-mesh is derived from an underlying primal mesh as median and/or voronoi dual, and is comprised of polyhedron cells. Grid generation methods, generally employ primal-cells to mesh a geometry. For example a structured-mesh is generated by employing hexahedra as grid elements [82], whereas unstructured meshing is carried out using tetrahedra cells [34, 85, 86], and hybrid mesh generation involves, e.g., prisms for boundary layer meshing together with tetrahedron grid elements for meshing regions away from the domain boundaries [38].

A cell-centered approximation uses the primal grid cells as control-volumes, while a vertex-centered approximation uses the dual-cells, making the choice of control-volume discretization dependent, this has a critical impact on the grid generation methods presented in this work. All flux approximation schemes used here are control volume distributed (CVD), i.e. employ a piecewise constant representation of rock properties over the grid control-volumes, with flow variables defined at control volume nodes or control-points (e.g. control-volume centroids). The two-point flux approximation (TPFA) is still most widely used in reservoir simulation due to its simplicity e.g. [6, 16, 2, 11, 40]. However, due to the limited range of applicability of the TPFA scheme (discussed below) more robust control-volume distributed multi-point flux approximation (CVD-MPFA) schemes have been developed, cell-centered CVD-MPFA schemes are presented in [16, 19, 18, 27, 26], other cell-centered CVD-MPFA related methods are presented in [1, 2, 88, 47] and cell-vertex (dual-mesh) CVD-MPFA schemes are presented in [18, 20, 21]. Unstructured mesh generation techniques are broadly classified into two categories: the advancing front method; and Delaunay triangulation [46, 63, 64]. The advancing front method provides an optimal point placement strategy and generates quality meshes. The advancing front method constructs a mesh by generating each element one at a time, where in order to validate each newly created element a check for intersection with existing elements is required [46]. Due to these reasons the advancing front method is not only inefficient but also suffers from robustness issues. Delaunay triangulation (DT) satisfies the empty circumsphere property (Delaunay criterion), i.e.,

every simplex (tetra) constituting a Delaunay grid does not contain any other mesh point, within its circumsphere drawn [85, 32]. Delaunay triangulations have the desirable locally orthogonal PErpendicular BIsectional (PEBI) property which is required by the industry standard two-point flux approximation for consistency when applied to isotropic fields or on k-orthogonal grids [6, 16]. In Delaunay mesh generation each point is triangulated one at a time generating multiple elements. It is well established that the Delaunay criterion has a sound mathematical basis, while its counter part, the advancing front method provides optimal point placement [64]. The idea to combine these two methods into one technique was introduced in the nineties [67, 63, 64]. In such a combined technique field points are introduced in a manner similar to the advancing front method, while their connections are improved by enforcing the Delaunay criterion [63]. The advancing front method used in conjunction with the Delaunay criterion both provides optimal point placement, and simplifies boundary aligned grid generation. There are several algorithms for construction of Delaunay triangulation [45, 30, 25], among others the incremental insertion [77, 8, 87, 31] is the most widely used technique. It is a simple and flexible technique in that its extension to higher space dimensions is relatively straight forward [82]. The two variants of incremental insertion algorithm, namely Watson's [87] and Green-Sibson's [31] method, are the most commonly employed algorithms for construction of Delaunay triangulation. The Green-Sibson's algorithm is more general in the sense that it can be used with any user defined connection optimization criterion to construct a data dependent triangulation [8]. In this work, we employ Green-Sibson's [31], used in conjunction with the advancing front point placement.

In this paper following the introduction, methods are presented for generating primal-cell grids for cell-centred methods and dual-cell grids for vertex-centred methods in section 2, where in particular gridding, boundary surface protection and curve protection procedures are described (in five key steps in subsections and flow chart displayed in Figure 2) that ensure both primal and dual-cell methods honour interior geological boundaries, and perforated grid

blocks (wells). The methods are illustrated with a well-fault interface example in section 3. A brief summary of CVD-MPFA methods together with a measure of M-matrix violation is then presented in section 4. This is followed by the results in section 5, where example primal and dual cell grids are presented together with results that provide comparisons in performance of the corresponding cell-centred and vertex-centered CVD-MPFA flux approximation schemes. A summary of the grid generation methods and CVD-MPFA comparisons is given section 6. Finally, we close with conclusions in section 7.

2. Proposed grid generation methods

In this work geological feature based primal and dual grid generation is presented for two groups of features [55, 56, 57, 59]. The first group involves domains that may include geological layers, pinch-outs, fractures and/or faults, and the second group involves well distributions. The primal and dual grid types are illustrated in Figure 1 and the five key steps involved in the proposed grid generation are summarized in the flowchart of Figure 2, and are detailed in the subsequent subsections that follow below.

Primal cell feature based grids are generated for cell-centred methods, with primal cell-faces (control-volume faces) aligned with geological boundaries. Boundary preservation is ensured by the novel use of special protection spheres, and illustrated for surface meshing with reference to Figure 1(a). In the empty mesh (described below subsection 2.4) protection spheres enclose the surface triangulation simplexes so that the surface definition is retained without any part of the surface triangulation being reconnected when volume meshing takes place. A formal statement of protection sphere properties is captured in the theorem of Appendix A. Volume meshing is performed such that field points are introduced so as to avoid invading protection spheres and obey the Delaunay criterion, ensuring the mesh is guaranteed to be a DT. However in contrast for deviated wells special local grid cell generation is required in order to preserve the well trajectories (so as to remain cell-centred on the primal mesh), which we call

a halo. This is illustrated in Figure 1(b), where in this case the halo cells are hexahedra. Introduction of a halo necessitates the use of other cell types to generate a local halo interface with the main grid, resulting in polyhedra (below) and consequently the DT property is relaxed locally. In the absence of wells the grid would be comprised of a purely tetrahedral DT mesh with the PEBI property [51, 64].

Dual-cell feature based grids are generated for vertex-centred methods such that dual-cell faces (i.e. control-volume faces) are aligned with the geological boundary surfaces, which is achieved via the use of surface enclosing halo cells. Thus boundary aligned grids are generated while primal grid vertices are not placed on interior geological boundaries, enabling vertex-centred methods to maintain the control-volume distributed property. We illustrate dual-cell surface meshing with reference to Figure 1(c), which shows a halo protected mesh comprised of prismatic cells (polygonal prisms) and polyhedral dual cells. Pyramids are used to provide transition from quad faces of the halos, and triangular faces of the outer tetra mesh. For the local non-tetra mesh, it is hard to ensure that the circumsphere of every element (prism, pyramid and/or hexahedron) is empty [13]. In order to design a robust halo construction procedure, the PEBI property is relaxed for halo elements only, however away from halos tetrahedra are used as grid elements and are ensured to have the PEBI property via the Delaunay criterion. Gridding of well trajectories is more straight forward in dual grid generation, as they are defined by primal grid nodes (vertices), Figure 1(d) with protection spheres ensuring their preservation under the action of volume meshing and a DT is ensured.

Thus both primal and dual-cell grids are generated such that their control volume faces honour geological boundaries yielding boundary aligned grids (BAGs), while for wells the grid nodes (or control-points) are aligned such that when joined sequentially the control points retrieve the well-trajectories, and are called well aligned grids (WAGs). The respective use of protection spheres and halos in these boundary preserving grid generation methods are a key contribution of this work and further details are given below.

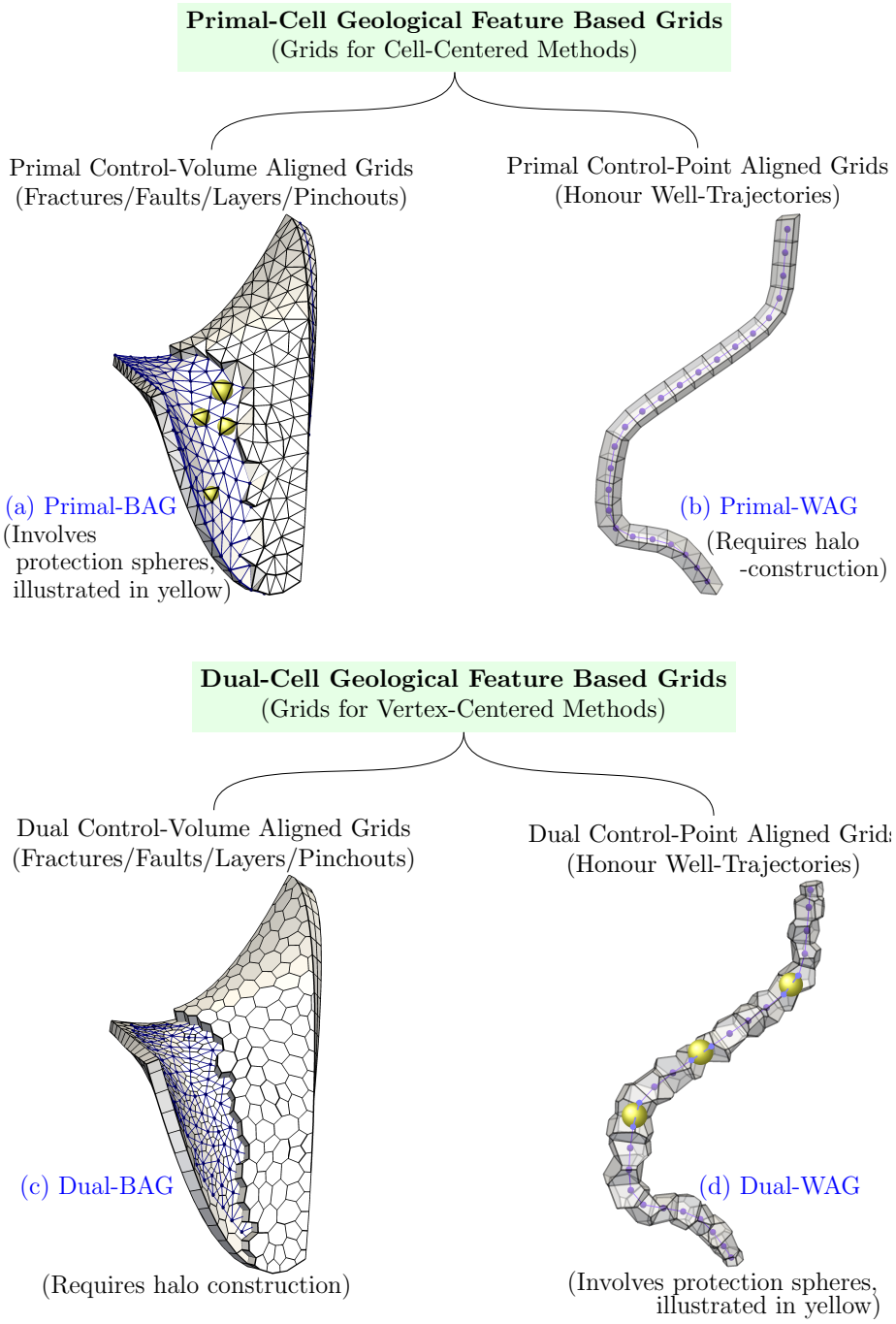

Figure 1: Classification of geological feature based grids, i.e., geological feature/boundary aligned (BAG) and well-aligned grids(WAG) both with respect to primal and dual cells.

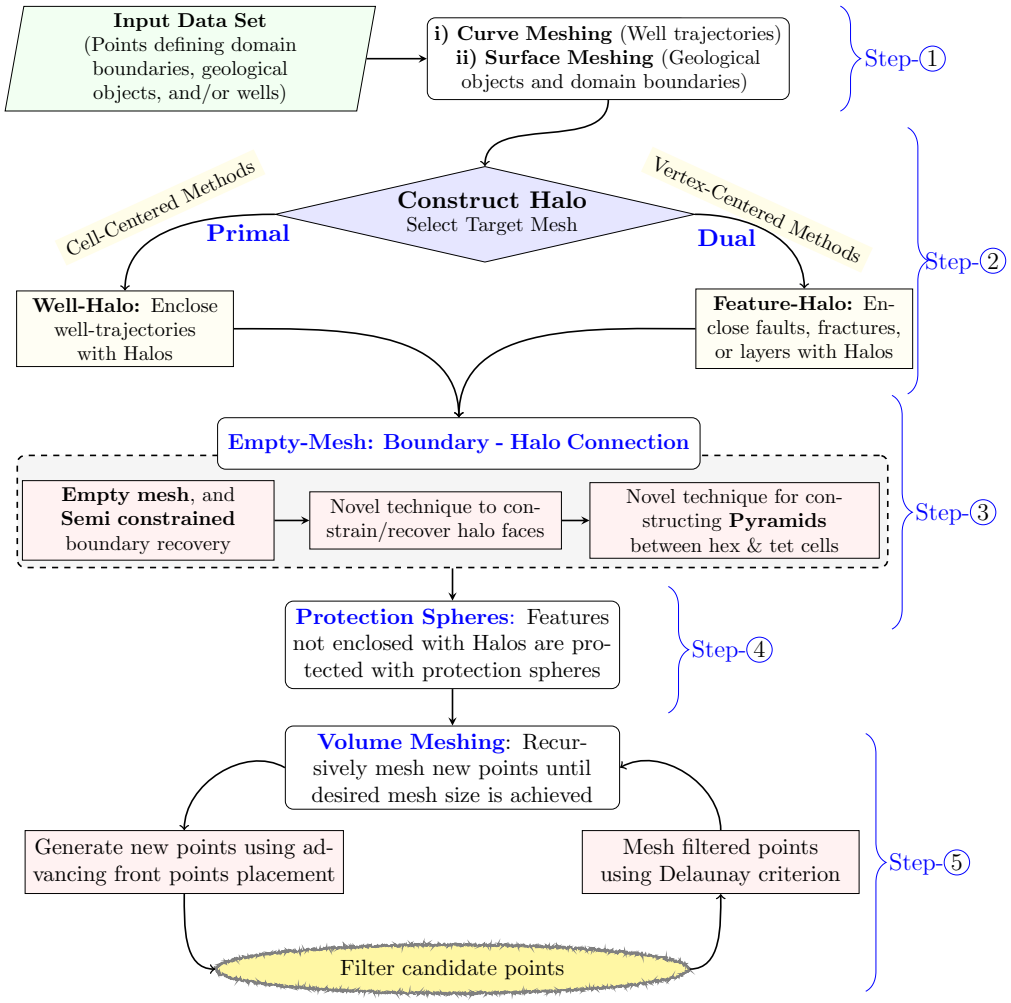

Figure 2: Key steps involved in the proposed method for generating boundary and well aligned grid.

2.1. Step-1: Curve and Surface meshing

Well-trajectories are characterized by three dimensional curves and embedded after being discretized using one dimensional curve linearization [49, 60], i.e., as a series of line segments, which when joined sequentially give rise to well-paths. Surface meshing techniques [48] are employed to construct a triangular surface-mesh of domain boundaries and of surfaces relating to geological objects. In this work, parametric surface meshing [83, 60] is used to mesh domain boundaries and geological objects. Meshing a surface in mapped two dimensional (u, v) space requires the use of a metric [48, 23, 60]. In a mapped space a metric is a 2×2 tensor, derived from a three dimensional representation of the surface. The metric allows the curvature of the surface to be taken into consideration. Since the metric is in general an anisotropic tensor, in the mapped space an anisotropic triangulation is generated subject to anisotropic variation of the Delaunay criterion [32, 60]. Figure 3 displays the resulting anisotropic mesh generated in a unit square parametric space $[0, 1] \times [0, 1]$, together with the corresponding isotropic mesh in physical space. The surface mesh is used

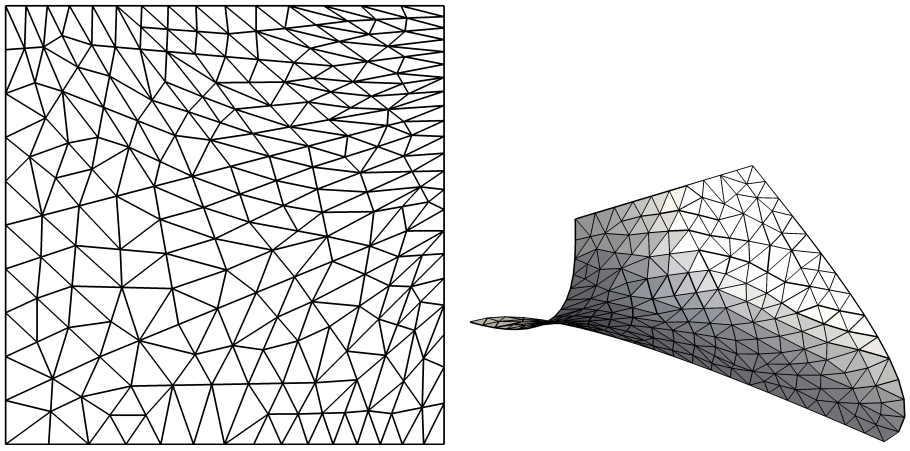

(a) Mesh of a surface in mapped space **(b) Isotropic mesh in physical space**

Figure 3: Anisotropic meshing in parametric (mapped) space (u, v), and corresponding mesh in the physical space.

directly in primal grid generation, with protection spheres enclosing surface grid

cells (in the corresponding empty mesh, e.g. see subsection 2.4) ensuring the surface triangulation is not violated when DT of the volume takes place. For the dual mesh, halo cells are introduced so as to enclose the surface, prior to the definition of the dual.

2.2. Step-2: Halo construction

The next step involves halo construction, which is performed by enclosing geological boundary surfaces and/or wells with prismatic-cells (polygonal prisms) such that actual features are retrieved as medial surfaces / curves derived from the halo elements. This is applied to well-paths for a cell-centred method and to geological objects for a vertex-centred method. A summary is given below with further details in appendix B and C.

2.2.1. Halos enclosing well-paths: for cell-centred method only

Geological reservoirs often have a layered structure, and well-trajectories traversing through the layers penetrate into the reservoir domain. When generating grids for use with cell-centred methods, multilateral well trajectories must be enclosed by protecting them with halos. To elucidate halo construction, consider a well-path discretely defined by a point set displayed in Figure 4a. At the points where a well-path intersects the first geological layer, a polygon located in the layer is constructed with its centroid positioned at the well intersection point. For the selected case two polygons (quads) located at the top and bottom surfaces are constructed such that their centroids meet at the intersection points of the well-path, with the respective surfaces, e.g., see Figure 8a. To start with halo construction, using the above constructed polygons, spears comprised of pyramids (or in general cones) are first built as shown in Figure 4a. A halo is propagated via spear pyramids which enables sequential hexahedra cell construction, displayed in 4b. The spears are propagated until the spear heads meet at a single point, called a junction point, e.g., see Figure 4c(left). Finally, the spear heads are opened to fully enclose features by the resulting hexahedron halo, as shown in Figure 4c(right). Figure 4c (right) also shows the medial curve

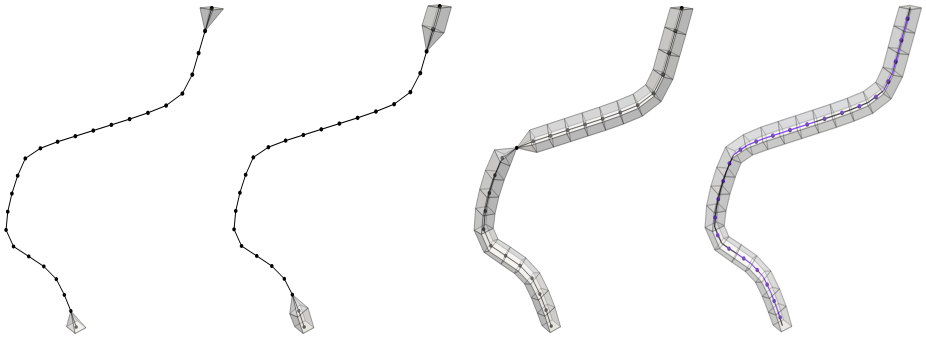

(a) Spear construction **(b) Advance spear constructing each hexahedron 1-1** **(c) Merge spear ends to fully enclose well-trajectory with halo**

Figure 4: Procedure to protect well-paths by enclosing them with hexahedron halo.

characterizing an honoured well-path in close proximity.

The procedure to sweep a polygon along a well-path is given in appendix B and is summarized (referring to figures in appendix B) in the following steps:

- *Translation:* Translate a sweeping polygon, i.e., base of the spear (pyramid), to the summit-node of the pyramid along the well-trajectory, as shown in Figure 20a.

- *Projection:* Project the translated swept polygon on to a plane passing through the summit-node, defined by the normal taken as an average of edge vectors emanating from the summit-node, i.e., bisection plane of edges meeting at the summit node (Figure 20b).

- *Size correction:* Ensure that the size of the projected polygon matches the size of reference polygon, i.e., to the base of the pyramid, this step is displayed in Figure 20c.

- *Propagating spear:* A new polygon is constructed, by sweeping the base of the existing spear element to its summit node. There is a one-one correspondence between a newly generated swept polygon and the base of

the existing pyramid (spear). This allows construction of a hexahedron together with a pyramid (spear) required for propagation, as displayed in Figure 20d.

2.2.2. Halo construction enclosing geological boundary surfaces: for vertex-centred method only

When generating grids for use with vertex-centred methods, surfaces characterizing geological objects are enclosed with halos, such that the input surface is retrieved as a medial surface of the halo elements. Before starting halo construction, for every surface mesh point a marching vector and marching step size are established. The marching vectors are defined by averaging normals to the surface-mesh triangles sharing the surface mesh point to be enclosed with a halo, e.g. see Figure 21.A marching vector constructed by averaging face normals may intersect with other neighbouring marching vectors. A variant of Laplacian smoothing, can be used to smooth the marching vector, such that it falls in the visibility cone [38] associated with the point being split, and also to resolve any possible intersection with neighbouring normals. For every surface mesh point the step-size assumed is representative of the average length of edges of the surface mesh sharing the point, limited by a user defined scale factor. To ensure formation of valid elements, the scale-factor can be locally modified. Initially the surface is comprised of triangles, operating on every surface mesh point(p) which is split into an edge ($p\bar{}q$), and the mesh is locally modified. The insertion of an edge in a background mesh comprised of triangles, tets, pyramids and/or prisms, also requires the use of tets, pyramids, and/or prisms. The key steps involved in enclosing a surface by protecting it with a halo are:

- *Cluster of point p:* Find group of elements (triangles, tets, pyramids and/or prisms) sharing point p, called the ball (cluster) of p
- *Star-shaped polyhedron:* Derive a star-shaped polyhedron (SSP) by deleting repeated interior edges, triangles and/or quads in the ball of p.

- *Split point into an edge:* Using the associated marching vector, point p is split by pushing point p downward generating a new point q and modifying p to p' by pushing it upward. The marching vectors are limited by step size, after splitting every point p into an edge $(\bar{p'q})$.
- *Re-mesh star-shaped polyhedron:* Re-triangulate the star-shaped polyhedron by connecting its edges/faces (tri/quad) to the edge $(\bar{p'q})$ in a consistent manner, generating tetrahedrons, pyramids and/or prisms. Further details relating how to re-mesh a SSP is given in appendix C.

Next we demonstrate the new method by honouring the surface displayed in Figure 3b with respect to dual-cells. Following the above procedure the surface is enclosed with a halo as displayed in Figure 5a. The medial surface of the halo corresponds to the input surface, e.g., see Figure 5b (centroid-dual) and is honoured with respect to the dual-cell faces. Salient features of the proposed

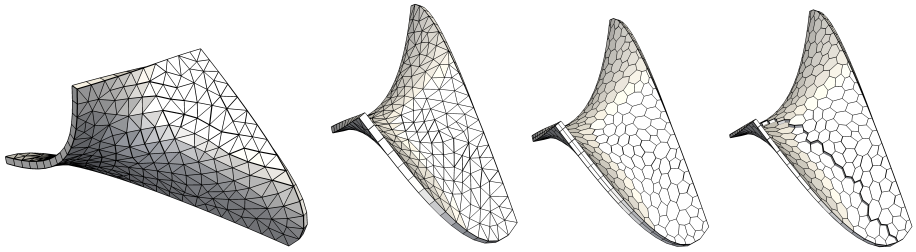

(a) Halo constructed around a representative feature shown in Figure 3b

(b) Centroid-dual of the halo protected primal-mesh (Figure 5a)

Figure 5: Geological features(fault/layer/fracture) in a dual-configuration are honoured by protecting them with halos constructed such that the medial surface of the halo corresponds to the embedded feature in close proximity.

halo construction method are given below:

- Operation on each point one by one in an unstructured manner and can also be used for 2.5D grid generation applications.
- Bi-directional marching thereby splitting points constituting the underlying surface by moving them in upward and downward directions, such

that the input surface can be retrieved as a medial surface of the halo elements.

- Operating on the star-shaped polyhedron associated with each point ensures visibility of the point (split-edge) with respect to edges/faces of the star-shaped polyhedron, yielding a valid grid.
- A quality and/or consistency check (is implemented), resolving intersection among the marching vectors, and allows changing marching vectors locally to avoid formation of self intersecting tangling elements.
- When halo construction is in transition, in addition to prisms the method involves the use of pyramids and tetrahedrons. The points where geological features intersect are treated via the use of spears comprising of tetrahedrons and pyramids.

2.3. Step-3: Empty-Mesh A: Boundary - Halo Connection

The first stage of Delaunay mesh generation involves connecting outer boundary nodes with interior boundary nodes and/or halo nodes creating what is termed an empty mesh. In this section we describe connection to halos (Empty-Mesh A). Connection to boundaries is described in Step 4 (Empty-Mesh B). Surface and curve meshing together with halo enclosure is performed a-priori. This results in a predefined data set and connectivity defining boundaries, halos, geological objects, and wells. Halos enclosing wells and/or geological objects are comprised of prismatic cells with quad (polygonal) faces. For Delaunay meshing and to recover halo faces (as a concatenation of simplexes), it is a prerequisite to subdivide any non-simplex external face into simplexes. Delaunay empty mesh generation involves the triangulation of a convex hull [14, 51] connecting a predefined data set. The empty-mesh is generated by employing an incremental insertion algorithm used in conjunction with the insphere criterion [64]. In Delaunay triangulation connections are established such that none of the spheres circumscribing simplexes contain any site in their interiors, but it cannot be guaranteed that connections between the given point set are present in a prescribed manner [85]. Consequently, integrity of the input boundaries, halo(s),

and/or curves can not be guaranteed. Therefore, it is mandatory to couple Delaunay triangulation algorithms with a boundary/feature recovery technique(s). This limitation of the Delaunay meshing is well known, and methods have been described [50, 85, 86] which can be employed to retrieve missing boundary connections.

2.3.1. Semi-constrained feature recovery supported by Steiner points

In three dimensions boundary recovery involves retrieving missing edges (that define predefined surfaces and curves), this is followed by face recovery, i.e., recovering the triangular surfaces. Two methods used to constrain a mesh to honour features/boundaries are: 1) conformal (local refinement) or stitching; and 2) non-conformal (local reconnection with/without Steiner points) recovery. Conformal boundary recovery is achieved with the use of additional points, called Steiner points, introduced recursively splitting missing connections (edges and/or faces), e.g., see [37, 85]. The conformal boundary recovery technique operates in an iterative manner, wherein during every iteration after ensuring integrity of edges, face recovery is performed, and missing faces are recovered, as a concatenation of sub-edges and/or sub-faces supported by the Steiner point(s). In the conformal recovery technique new points are triangulated subject to the Delaunay criterion, and the resulting boundary honoured grid will have the PEBI property [51, 58]. Boundary recovery by local-reconnection / swapping relies on edge and/or face-swaps used to retrieve missing connections. In contrast to the two dimensional constrained boundary recovery technique [79], in three dimensions there is no theoretical basis for the success of local reconnection methods, this is due to the existence of Schönhardt polyhedron [32, 50, 72, 86]. A Schönhardt configuration, can not be triangulated without adding a new point, thus success of constrained boundary recovery relies on the occasional insertion of Steiner points. Boundary recovery involving local-reconnection used in conjunction with Steiner point insertion, is a semi-constrained boundary recovery technique. In this work:

- For primal grids curves corresponding to wells are recovered by using the

stitching conformal recovery technique, and have PEBI property.

- For dual-grids, face recovery is required for boundaries and in particular for halos, as a concatenation of simplexes without Steiner points. To this end, at first semi-constrained face recovery with minimal use of Steiner points is performed, this is followed by fully constrained recovery achieved by suppressing Steiner points. A novel technique to suppress Steiner points is described below (section 2.3.2).

With semi-constrained recovery, missing faces of boundaries and those of halos have been recovered as a group of sub-faces (triangles) supported by Steiner point(s). At this point, the superfluous tetrahedrons including those formed inside the halo(s) and those outside the region of interest formed due to the convex bounding box, containing the given data set employed for the incremental insertion algorithm to carry out Delaunay triangulation are now deleted [32]. This will simplify the empty mesh for further processing, and may also remove some Steiner point(s). Next to fill a halo channel with predefined halo elements, 1) Steiner points must be removed; and 2) Pyramids acting as transition elements connecting triangular faces of tetra and quad faces of halo elements should be constructed.

2.3.2. Novel technique to suppress Steiner points & fully constrained feature recovery

Any Steiner point(s) interrupting the pre-defined connectivity of the halo elements must be removed. This demands fully constrained recovery without Steiner points. As described above in three dimensions fully constrained Delaunay triangulation can not be achieved by local reconnection alone, thus at first we perform semi-constrained recovery and then fully constrained recovery is achieved by suppressing Steiner point(s) ensuring connectivity of the input mesh or halo. To suppress a Steiner point we re-mesh its associated star-shaped (Bowyer-Watson's) polyhedron(SSP) locally, by projecting a Steiner point in a direction normal to the intersected edge and/or face inside the SSP, e.g., see

Figure 6. In a case where a Steiner point is locked, i.e., its movement in any direction renders one or more tetrahedral element(s) connected to it to be negative, then to ensure topology of quad faces of the halo hexahedron, low quality elements may form which are later exuded by local reconnection and/or smoothing. Figure 6 displays key steps involved, when suppressing a Steiner point, and are explained below:

- *Cluster sharing Steiner point(p):* Find the set of elements sharing the Steiner point(p) to be lifted, also called a ball/cluster of point p. Figure 6a displays the cluster of a Steiner point p introduced to honour a quad face of a halo hexahedron.

- *Star-shaped polyhedron*: A star-shaped polyhedron is derived from the cluster sharing Steiner point p, this is done by removing repeated interior faces of the elements constituting a cluster of the point p, e.g., see Figure 6b.

- *Lift the steiner point(p) and modified star-shaped polyhedron:* In order to recover an underlying quad face, as a set of two triangles, the Steiner point being suppressed is lifted in a direction normal to the underlying quad face, a distance limited by ensuring visibility of the lifted point with respect to faces of the associated star-shaped polyhedron. After the Steiner point is lifted, the underlying quad face is recovered as a set of two triangles, modifying the associated star-shaped polyhedron, e.g., see Figure 6c.

- *Re-meshing the modified star-shaped polyhedron:* Connecting the lifted Steiner point(p) to the faces of the modified star-shaped polyhedron, a set of new tetrahedrons defining the ball of point p is created, as shown in Figure 6d.

When suppressing Steiner points, a special case may be encountered and is described in Appendix D.

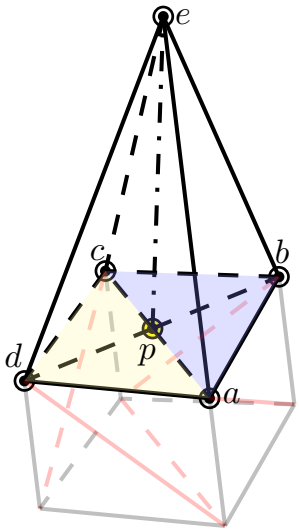

(a) A Steiner point(p) introduced to honour quad face $(abcd)$ of a halo-cell.

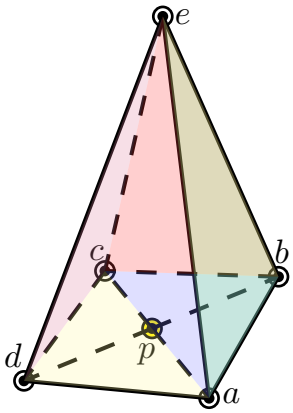

(b) Star-shaped polyhedron associated with Steiner point p, constructed by deleting interior faces $(\triangle pae, \triangle pbe, \triangle pce, \triangle pde)$ from the cluster of p.

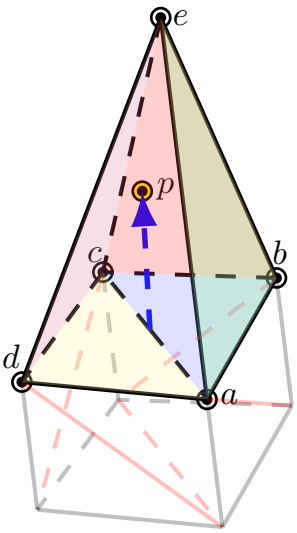

(c) Lift Steiner point & replace sub-diagonals of underlying quad face with a desired diagonal.

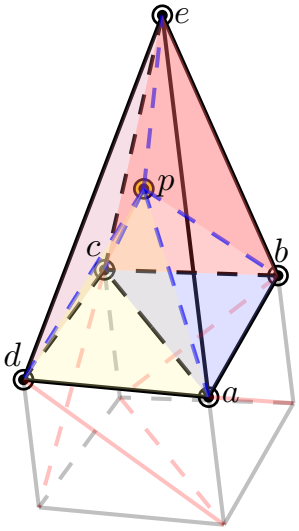

(d) Re-mesh star-shaped polyhedron, joining each of its faces to the lifted Steiner point

Figure 6: Procedure to suppress Steiner points, by lifting them in a direction normal to the underlying quad face.

2.3.3. Novel technique for constructing pyramids as transition elements & filling halo channel

After fully constrained recovery is achieved, in the empty mesh, each quad face of the halo exists with a diagonal subdividing it into two triangles. By joining each set of two such triangles the underlying quad faces are reconstructed. The empty mesh is comprised of tetrahedra, and therefore insertion of quad-faces over the halo surfaces, requires a transition from hexahedra (prisms) to the tetrahedra mesh. To establish connectivity between (hex) quad and (tet) triangular faces, pyramids are used as transition elements. Here, a novel technique to construct an unstructured pyramid layer abutting the halo quad faces, such that the underlying halo channel can be filled with hexahedra is used. To recover a quad face, the edge splitting it into two triangles is deleted, and a pyramid is constructed abutting the recovered quad-face. Figure 7 presents the pictorial representation highlighting key steps involved in constructing the pyramids as transition elements. For every edge that splits the underlying halo quad into two triangles, we operate in the following manner:

- *Edge cluster:* Find the set of elements (tets) sharing the edge (diagonal) subdividing an underlying halo quad face into two triangles, named edge cluster. Figure 7a displays an edge ac subdividing the halo quad($abcd$) into two triangles ($\triangle abc, \triangle acd$). There are three tetrahedrons sharing the edge ac, and these are $(abce, acdf, acef)$.

- *Star-shaped polyhedron:* Deleting repeated interior faces of the cells constituting a cluster of the edge to be removed, an associated star-shaped polyhedron (SSP) is derived, e.g., see Figure 7b.

- *Deleting edge and constructing quad-SSP:* By default a star-shaped polyhedron (SSP) is comprised of triangular faces, deleting the edge on the halo face at hand, the two triangular faces of the SSP sharing the edge are joined to construct a quad, yielding a modified star-shaped polyhedron having a quad face, called a quad-SSP.

- *Re-meshing a quad-SSP:* In order to construct a quality pyramid, a new point in a direction normal to the recovered quad face is introduced inside the quad-SSP, limited by a scale factor initially assumed as representative of spacing of points constituting the underlying quad, as displayed in Figure 7c. The scale factor is then limited by a distance ensuring local-convexity [64], i.e., visibility of the faces constituting the quad-SSP with respect to the point being introduced is ensured. The quad-SSP is then re-meshed by connecting the new point to the faces of the quad-SSP, creating a pyramid abutting the halo face and tets are generated when triangular faces of the quad-SSP are joined to the new point, e.g., see Figure 7d.

Since the quad-SSP is star-shaped with respect to points located on the associated edge [32], the proposed method for pyramid construction is robust. Appendix E describes special cases, that may be encountered when constructing pyramids as transition elements.

2.4. Step-4: Empty-Mesh B: Boundary - interior protection-sphere enclosed boundary connection

Empty mesh generation involves connecting outer boundaries to interior boundaries and halos. Connection to halos is described in Step-3: (Empty-Mesh A) which yields a predominately Delaunay grid. After connection with interior boundary nodes, and prior to volume meshing, in order to avoid swapping and to preserve integrity of feature boundary connectivity honoured/recovered in the empty mesh (Step-3), we introduce protection spheres (described above) that pass through the simplexes/segments constituting geological objects/wells. In volume mesh generation, integrity of features is maintained provided any new points encroaching the protection spheres are rejected. Protection spheres are used both in cell-centered and vertex-centered grid generation methods. In the former, protection spheres are used to retain triangular cell-faces aligned with geological boundary surfaces, and in the later protection spheres are used to protect cell-edges constituting well-path(s). Types of protection spheres with validity conditions for application are given in Appendix A.

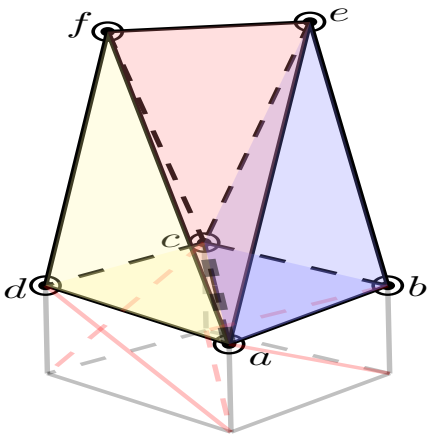

(a) Edge ac has three tetrahedrons associated with it $(abce, acdf, acef)$

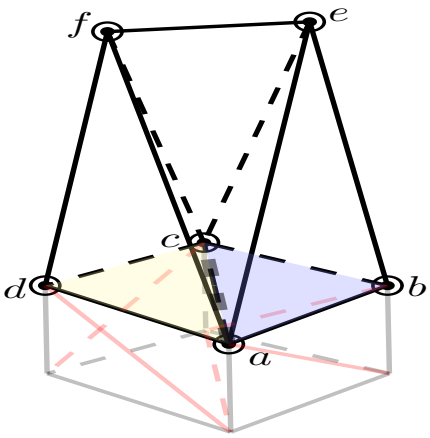

(b) Star-shaped polyhedron obtained after deleting repeated interior faces (ace, acf)

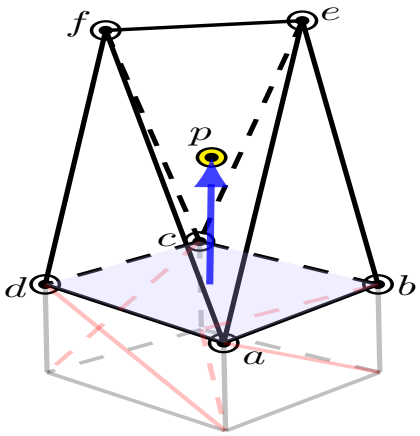

(c) Delete edge(ac), modify star-shaped polyhedron to have a quad$(abcd)$, and introduce a new point in a direction normal to quad face$(abcd)$.

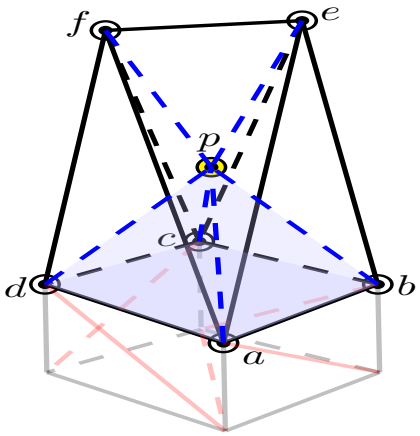

(d) Construct pyramid by joining quad face of star-shaped polyhedron(SSP) to new point and tetra from the tri-faces of the SSP.

Figure 7: Procedure to construct a pyramid transition element required to recover underlying quad face

2.5. Step-5: Feature honoured 3-D volume mesh

The above steps lead to the empty mesh, which is comprised of large low quality elements connecting far ends of domain boundaries, geological boundaries, surfaces and halos. In order to generate a quality well resolved grid leading to the three-dimensional volume mesh, the empty mesh is locally refined by introducing new (field) points. In order to start with field mesh generation in the empty mesh a metric (density distribution function) [63, 29, 49] is assigned to each point. For uniform isotropic meshing, a scalar value representative of boundary point spacing defines the metric. In the empty mesh quality elements, e.g., those constituting halos satisfy unit metric length approximately and are not refined. Field points are introduced using the advancing front method and triangulated subject to the Delaunay criterion iteratively until a unit metric length mesh [29] is generated. The candidate points introduced during each level are filtered to remove conflict with protection spheres, halo elements, pyramids, and existing previously generated points. In the general case the grid will be comprised of tetrahedra, prisms, pyramids and hexahedra. The dual mesh is generated by joining cell centroids (or circumcentres when inside tetra) to cell-face midpoints, which are joined in turn to cell-edge midpoints. The resulting subcells attached to a given grid vertex form a polyhedron which is the dual cell.

3. Examples: Boundary and well aligned grid generation

A multilateral well penetrating a representative faulted layer, Figure 8a, is selected to demonstrate the proposed grid generation methods. The five key steps of section 2 are followed in both cases with appropriate use of halos according to grid type following step 2. Surface meshing of the domain boundaries and fault is performed first for both grid types.

3.1. Grid generation for cell-centered methods

Cell-centered formulations have primal-cell faces aligned with geological boundary surfaces and halo cell-centers aligned with wells. After surface meshing (step

1) the multilateral well is enclosed with a halo comprised of primal-cells (prismatic cell type depends on constraints, here hexahedra are used) following step 2 as described in section 2.2.1, and illustrated in Figures 8a-8b. After halo construction, for mesh conformity, the halo sweep polygon(s) for well trajectories are made an integral part of the corresponding surface mesh together with local refinement. For step 3 (empty mesh A), non-triangular faces of halos are subdivided into triangles as shown in Figure 8c. For step 4 (empty mesh B), simplexes defining the embedded feature surface are protected by protection spheres, c.f. Appendix A. The empty mesh is generated, with surface and halo integrity ensured, with pyramids forming transition elements and the halo channels having prismatic-cells of predefined connectivity, e.g., see Figure 8d. The empty-mesh is then refined by triangulating new (field) points via the advancing front procedure of step 5. A cross-section of the resulting final mesh generated, is displayed in Figure 8e.

3.2. Dual grid generation for vertex-centered methods

Vertex-centered formulations have dual-cell faces aligned with geological boundary surfaces and primal grid vertices aligned with wells. After surface meshing (step 1) halo cells are generated to enclose the geological boundary surface following step 2 of section 2.2.2, with the fault boundary (Figure 8a) aligned with the dual-cell faces of the halo displayed in Figure 9a. Local refinement is performed around the intersection points of well trajectories with the surface, c.f. Figure 9a. The halo protected empty-mesh A (step 3) is displayed in Figure 9b, where integrity of the halo surface is ensured with pyramids forming protected transition elements (Figure 9b). Adjacent well trajectory nodes are enclosed by protection spheres in step 4 (empty-mesh B), also shown in Figure 9b, where the halo protected empty-mesh is displayed. The 3-D mesh is generated following step 5, a cross-section of the final halo protected surface and well-trajectory preserved primal mesh, is displayed in Figure 9c. The dual-mesh is then derived from the 3-D mesh of step 5 Figure 9c and displayed in Figure 10a. Note that faces of the dual-cells (polyhedrons) respect the embedded fault

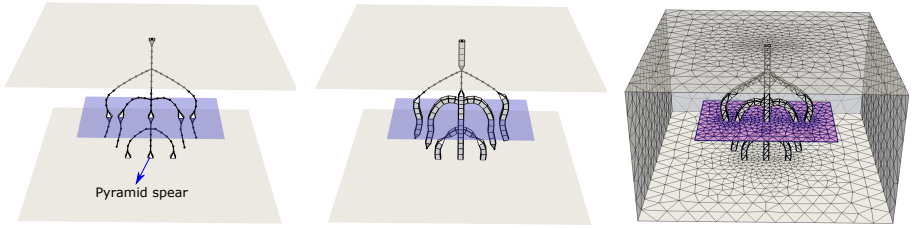

(a) Using underlying quads, pyramids are constructed as spears

(b) Propagate halo to enclose well-path

(c) Non-triangular faces of the halo are subdivided to triangles.

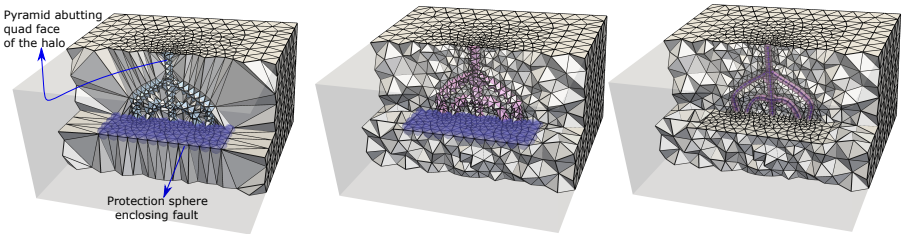

(d) Halo-protected BAG empty mesh

(e) Well-path enclosed boundary aligned final primal mesh

Figure 8: Primal-cell boundary and well-halo control-point aligned mesh

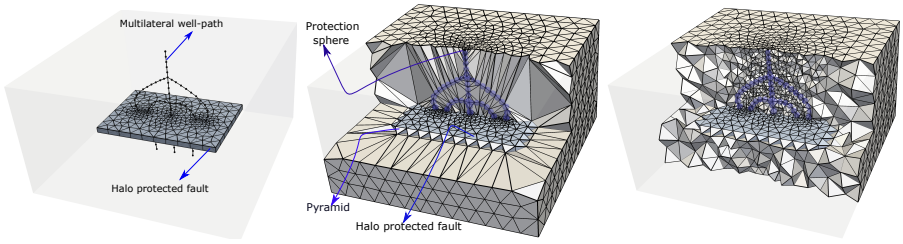

(a) Halo-protected fault and conformal discretization of the multilateral well-path intersecting synthetic fault

(b) Halo-protected empty primal mesh

(c) Boundary/feature enclosed well-path preserved final primal mesh

Figure 9: Dual-cell boundary and well aligned grid generation (required in cell-vertex method)

and the well-trajectory is retrieved by joining the centroids (i.e. vertices) of the polyhedron (dual) cells enclosing the well-path in a sequential manner, Figure 10b.

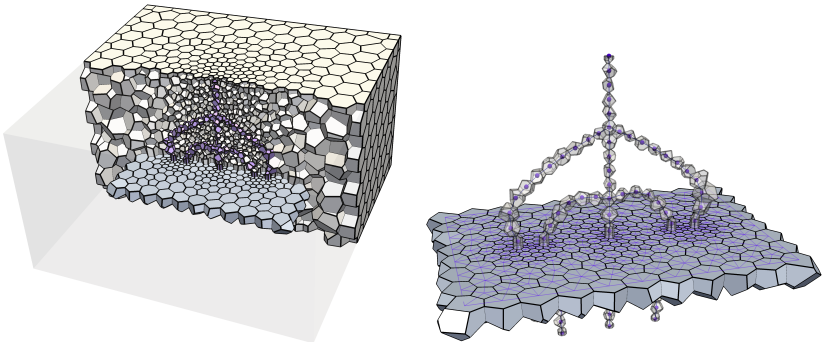

(a) Cross-sections of the dual-mesh **(b) Close of the dual-mesh showing dual-cells honoring both fault and well**

Figure 10: Cross-section and close up of dual-cell boundary and well aligned grid (cell-vertex mesh), derived from Figure 9.

4. CVD-MPFA, flow equations and measure of M-matrix violation

A brief review of CVD-MPFA schemes for pressure equation discretization is now given. The constraints and consequences for generating unstructured grids that are compatible with CVD-MPFA have been discussed at length in the above sections, however in contrasting the methods; With the exception of wells, the cell centred method can be used with more conventional primal grid generation provided interior boundaries are honoured, while the vertex-centred method requires a non-conventional dual grid generation method, while for wells the converse is true. Two important distinctions between cell-centred and vertex-centred methods arise on unstructured grids. First, while for structured meshes the number of primal and dual cells are basically equivalent with an off-set for boundaries, for unstructured grids (tetrahedra) the number of cells (tets) are between 5 and 6 times the number of mesh vertices. This is easily envisaged by

constructing an unstructured mesh from a background structured mesh, in 3-D this requires subdividing each hexahedron into 5 or 6 tetrahedrons, providing a rough estimate of the ratio which can vary on general unstructured grids, in this work the ratio is between approximately 4 and 5. Consequently the cell-centered formulation involves many more degrees of freedom, and is thus more computationally expensive, but might be expected to resolve flow fields more accurately. Secondly for the cell-centred method, the local flux molecule depends on the number of cells attached to a vertex, while the vertex-centred local flux molecule only depends upon the vertices of the primal cell, and consequently the vertex-centred method is relatively compact, with much smaller bandwidth when the discretization matrix is assembled, this is illustrated in two-dimensions in [57].

Pressure equation: The pressure equation arises from mass conservation together with Darcy's law and is written in integral form as:

$$-\int_{\Omega} \nabla.(K\nabla\phi)d\Omega = q \tag{1}$$

where ϕ represents field pressure; ∇ is the gradient operator, K is the elliptic symmetric permeability tensor; q is the source term, which is zero away from well sources or sinks. The finite-volume formulation begins with the use of the Gauss divergence theorem to integrate Equation 1, over a control-volume Ω. After integration Equation 1 is then written as

$$-\oint (K\nabla\phi) \bullet \vec{n} d\Gamma = -\sum_{i=1}^{n_f} \int_{\Delta\Omega_i} (K\nabla\phi \bullet \vec{n_i}) d\Gamma = q \tag{2}$$

where Γ corresponds to the boundary of control-volume Ω, $\Delta\Omega_i$ is the i^{th} face of the control-volume and n_f is the number of faces; $\vec{n_i}$ is the outward unit normal to face i as shown in Figure 11. The resolution of Darcy velocity $-K\nabla\phi$ along the unit normal n_i is called the Darcy-flux through face i.

Approximation of Darcy-flux is a key step in a finite-volume formulation and many approximations have been proposed, here we use the control-volume distributed multi-point flux approximation (CVD-MPFA) formulation. Cell-

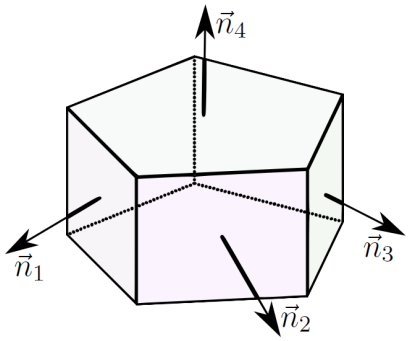

Figure 11: Representative polyhedral control volume..

centred CVD-MPFA formulations are presented in [16, 19, 26, 27, 3, 4, 57], and CVD-MPFA related cell-centered methods are presented in [2, 1, 88, 47, 42]. Vertex-centred CVD-MPFA formulations are presented in [18, 20, 21, 70, 57].

CVD-MPFA schemes work directly with the integral form of the flow equations and are optimal in the sense that they employ a single primal discrete pressure per control-volume, and provide consistent flux-continuous locally conservative approximations of the pressure equation for any permeability tensor and grid type, while satisfying local pressure and normal flux continuity conditions. The continuity conditions imposed around every cluster point, e.g., [26, 57], leads to an increased pressure support with wider matrix bandwidth compared to the standard TPFA scheme, but crucially retains the same number of unknown discrete pressures or degrees of freedom. However the TPFA scheme has O(1) error in flux and is generally inconsistent unless the grid is K-orthogonal [6, 16]. We note that alternative CVD-MPFA related methods have been proposed [68] which involves a hybrid approximation and [53] which imposes a maximum principle via a non-linear formulation. In terms of other methods, we note that the control-volume finite element method (CVFE) [24, 61] uses the same vertex degrees of freedom as the cell-vertex CVD-MPFA method, however unlike CVD-MPFA, CVFE is not flux continuous across interfaces separating jumps in permeability, which can lead to loss of flow resolution compared to CVD-MPFA [17]. We note that all other methods that rival CVD-MPFA

in terms of consistency, flux continuity and linearity depend on a much larger number of degrees of freedom and consequently yield much larger assembled matrices. For example on a 3-D structured grid mixed finite element methods, e.g., see [7, 74, 12] require four times as many degrees of freedom. The mixed hybrid finite-element method (MHFEM) [10] and mimetic methods [52] only depend on control-volume face values and have an SPD matrix. However, while reducing the degrees of freedom compared to the original mixed methods, with the traditional control-volume centred pressures now removed, MHFEM still involve three times the degrees of freedom when compared to the CVD-MPFA formulations in 3D, while CVD-MPFA only depends upon the traditional control-volume centred pressures.

CVD-MPFA schemes divide into two types, namely triangular(2D) / tetrahedral(3D) pressure support (TPS), and full pressure support (FPS) schemes. CVD-MPFA (TPS) schemes are parameterized by quadrature q. The quadrature point q can be selected anywhere between the cluster vertex($q = 0$) (but not at the cluster vertex which would be singular) and edge mid point(q=1) with $0 < q \leq 1$, where continuity of flux is imposed. We note for cell centred methods the default ($q = 1.0$) corresponds to standard CVD-MPFA ([16, 1]), and ($q = 2/3$) defines the SPD variant for arbitrary triangle cell meshes [26]. Note that anisotropic quadrature is also possible e.g. with FPS [20], but not explored here.

Measure of M-matrix Violation: An M-matrix ensures a local discrete maximum principle (LDMP) and that the discrete solution is free of spurious oscillations, however as with all linear schemes, CVD-MPFA schemes have conditional M-matrices [19, 16], and M-matrix violation can occur for sufficiently strong full-tensor problems. The degree of M-matrix violation is measured, by comparing for local diagonal dominance violation of the corresponding discrete matrix. For every row of a discrete matrix $\mathbf{A}$, the number of positive off-diagonals and maximum positive off-diagonal relative to the positive diagonal-term i.e. $max(a_{i \neq j})/a_{ii}$ for $a_{ij} > 0$ are computed [57]. L_∞ and L_2 norms together with arithmetic mean($\bar{x}$) of all row violations are used as representative measures of

M-matrix violation.

5. Numerical results

The benefits of dual-meshing over primal meshing for the respective CVD-MPFA formulations was recently demonstrated by [57] in two-dimensions with the aid of a new dual-mesh generator which is essential for a CVD-MPFA cell-vertex formulation. Previous comparative studies of other cell-centered and vertex-centered methods for subsurface flow have been undertaken [22, 35]. Here, in addition to developing and demonstrating novel grid generation methods compatible with CVD-MPFA in three-dimensions, a comparative performance of cell-centered versus vertex-centered CVD-MPFA schemes is presented together with measures of the degree of M-matrix violation. For comparison purposes the meshes employed are designed to be comparable in the primal framework and for vertex-centered simulations the median-duals act as control-volumes, unless stated otherwise. A number of test cases are presented including reservoirs with strongly anisotropic permeability fields.

5.1. Case-1: Cell-centred versus vertex-centered TPFA and CVD-MPFA on mixed element meshes

This test case is designed to simulate a linear pressure field, so as to validate the implementation of cell-centered and vertex-centered TPFA and CVD-MPFAs formulations in 3-D. We simulate the linear pressure field, on a cubical domain, i.e., $\Omega = [0,1] \times [0,1] \times [0,0.5]$, governed by homogeneous permeability tensor $K = I$. The analytical solution governing linear pressure field is defined by: $\phi(x,y,z) = x + y + z + 1$. The system is closed by prescribing Dirichlet boundary conditions on the sides of the cubic domain, imposed from the exact solution. To simulate the flow field, the grid employed is displayed in Figure 12, and is comprised of prisms, hexahedra and hexagonal-prisms. In cell-centered and vertex-centered configurations the centroid is used as the approximation and dual-point respectively, unless stated otherwise. In cell-centered

mode primal-cells act as control volumes, whereas in the vertex-centered mode control-volumes are dual polyhedrons constructed around primal mesh vertices using primal-cell centroid dual-points, as shown in Figure 12b. The number of control-volumes used in cell-centered and vertex-centered modes are 4869 and 3970 respectively. The L_2 norm of pressure field error is used to compute deviation from the true solution and is given by equation 3, where n_{cv} are the number of control volumes with V_i, ϕ_i and ϕ_{h_i} are volume, exact pressure and numerical pressure solution respectively for control volume i and e_h denotes the error.

$$L_2(e_h) = \left(\frac{\sum_{i=1}^{n_{cv}} (V_i(\phi_{h_i} - \phi_i)^2)}{\sum_{i=1}^{n_{cv}} V_i} \right)^{1/2} \tag{3}$$

5.1.1. Cell-centred vs vertex-centered CVD-MPFA

Both cell-centered and vertex-centered TPS and FPS schemes are employed to simulate the linear flow field, results with $L_2(e_h)$ for pressure fields are displayed in Table 1. The results substantiate that both cell-centered and vertex-centered formulations resolve the linear flow field exactly [19, 69].

Scheme	Formulation	$L_2(e_h)$ pressure
TPFA	cell-centered	2.9407×10^{-03}
	vertex-centered	3.2135×10^{-03}
TPS	cell-centered	2.2329×10^{-14}
	vertex-centered	5.4651×10^{-14}
FPS	cell-centered	3.8166×10^{-14}
	vertex-centered	5.4682×10^{-14}

Table 1: $L_2(e_h)$ of pressure for cell-centered vs vertex-centered TPFA and CVD-MPFA employed to simulate linear-flow field

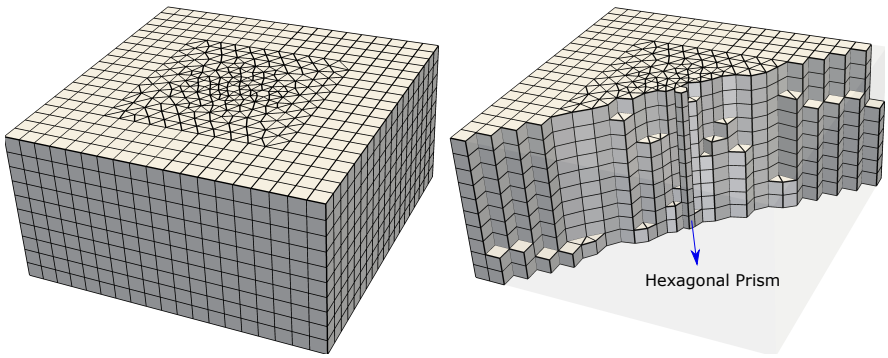

(a) Mixed elements hybrid mesh comrpising of 3970 points and 4869 polygonal prisms (3312 prisms + 1512 hexahedron + 45 hexagonal-prisms)

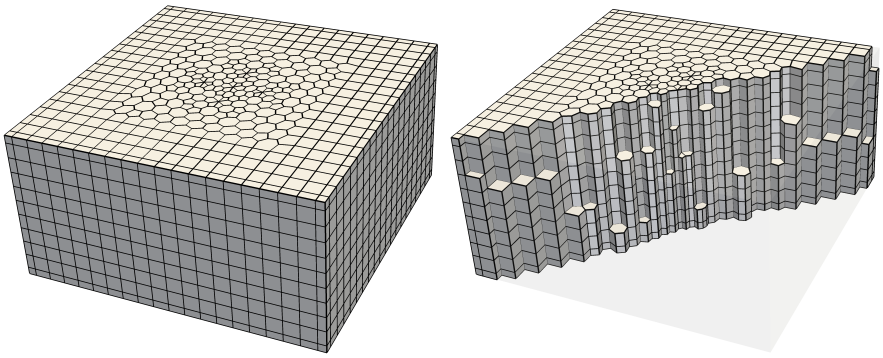

(b) Median dual derived from the prismatic primal mesh shown in 12a.

Figure 12: Grid (prismatic-cells) used for simulating pressure field case-1.

5.1.2. Cell-centred vs vertex-centered TPFA

For this case the industry standard two-point flux approximation (TPFA) is tested. Both cell-centered and vertex-centered TPFA are found to yield inconsistent approximations. This is because the grids (Figure 12) employed using the centroid as the approximation (cell-centered formulation) and dual-point (vertex-centered formulation) are not K-orthogonal. For an isotropic flow field the Delaunay-grid is K-orthogonal, provided the circumcentre is used as the approximation/dual point. Figure 13a displays the linear flow field resolved exactly by employing TPFA, simulated on an unstructured Delaunay triangulation with circumcentre as dual-point. However when the same unstructured grid is employed using the centroid as the dual-point an inconsistent approximation is obtained, e.g., see Figure 13b. Consistency of TPFA demands a K-Orthogonal mesh, which in the general case where meshes are comprised of general grid elements and flow domains have strong anisotropic permeability fields can not be ensured, and therefore TPFA has limited applications [84, 16].

5.2. Case-2: Discontinuous full-tensor test case with imposed vertical source and sink

This case contains internal intersecting boundaries and is selected to compare cell-centered versus vertex-centered CVD-MPFA formulations. A heterogeneous domain $\Omega = [0, 3] \times [0, 1] \times [0, 0.45]$, is embedded with a layer/fault system partitioning the computational domain into four distinct regions, e.g., see Figure 14. A piecewise constant permeability tensor is assumed in each sub-domain and its orientation is varied $\pm 30^{\circ}$, so as to define a discontinuous permeability field. Two vertical wells are located at opposite corners, i.e., $(0.75, 0.25)$ and $(2.25, 0.75)$, penetrates from the top to bottom of the domain. The wells are considered as geometrical objects with Dirichlet boundary conditions, assumed with pressure $\phi = 1$ and $\phi = -1$ defining source and sink. In order to close the system we specify homogeneous Dirichlet boundary conditions with pressure $\phi = 0$ on the sides, together with zero normal flow boundary conditions prescribed on the top and bottom of the domain. The permeability tensor across the sub-domains

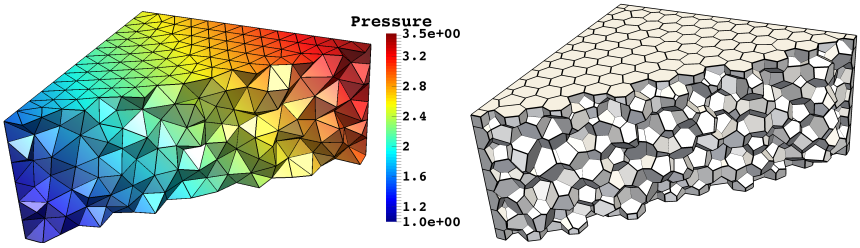

(a) Cross-section of vertex-centered TPFA with circumcentre as dual point (voronoi mesh) has $L_2(e_h) = 4.695 \times 10^{-15}$.

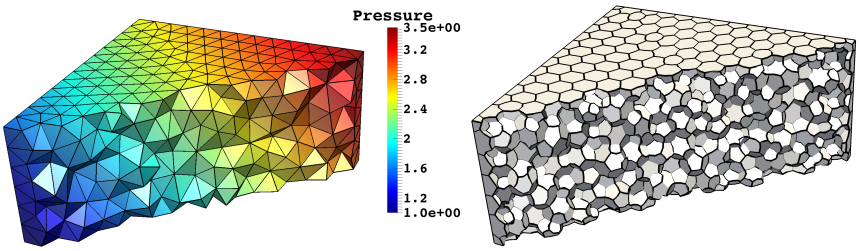

(b) Cross-section of vertex-centered TPFA with centroid as dual point (median-dual mesh) has $L_2(e_h) = 2.804 \times 10^{-03}$.

Figure 13: Vertex-centred TPFA on an unstructured Delaunay triangulation with centroid vs circumcentre as dual-point.

is discontinuous (defined below), and consequently to minimize discretization error feature based grids honouring both faults and well-paths are required. For a cell-centered formulation the primal-cells act as control-volumes, and the grid employed is generated by enclosing wells with halos and primal faces aligned to the internal boundaries, e.g., see Figure 14a. Whereas in a vertex-centered formulation the dual-cells are chosen as control-volumes. To honour features in the dual grid the internal boundaries require special treatment, using a prismatic halo construction as shown in Figure 14b. Halo construction enclosing a feature, is performed such that the actual feature can be retrieved as the medial surface of the halo elements as displayed in Figure 14b (right).

5.2.1. Case 2a: Anisotropy ratio=6

The permeability tensor with anisotropic ratio $k_{11}/k_{22} = 6$ and orientation $\theta = 30^\circ$ in xy plane, e.g., see Equation 4 is assigned to first and third subregions. In the second and fourth subregions the permeability tensor has the same anisotropic ratio however with different orientation $\theta = -30^\circ$ yielding negative off-diagonal coefficients, i.e., $k_{12} = k_{21} = -2.165$ and $k_{13} = k_{31} = -1$. First we test performance of cell-centered versus vertex-centered TPFA. TPFA does not yield a consistent solution, this is because the grid employed is not K-orthogonal, nevertheless the numerical solution is bounded and has a local discrete maximum principle (LDMP) [19, 53]. The TPFA solution displayed in Figure 15a has a LDMP, both in cell and vertex centred configurations. Next we compute the pressure field using the CVD-MPFA schemes. The resulting numerical pressure solutions are shown in Figure 15b. Both cell-centered and vertex-centered CVD-MPFA yield consistent well resolved pressure fields free of any visible spurious oscillations. However, M-matrix violation is observed for both cell-centered and vertex-centered CVD-MPFA-TPS, induced by the permeability tensor and grid, and is tabulated so as to provide a formal measure of violation as defined earlier, e.g., see Figure 15c. The table clearly shows that the cell-centered method has the worst violations. When comparing TPFA versus CVD-MPFA pressure fields 15, we note that as expected, TPFA does not

capture the anisotropy of pressure field due to the inherent inconsistency of the method in such cases.

$$K = \begin{pmatrix} 4.750 & 2.165 & 1.000 \\ 2.165 & 2.250 & 0.000 \\ 1.000 & 0.000 & 2.250 \end{pmatrix} \tag{4}$$

(a) Primal-cell boundary and well aligned grid (cross section), comprised of 9556 primal control volumes.

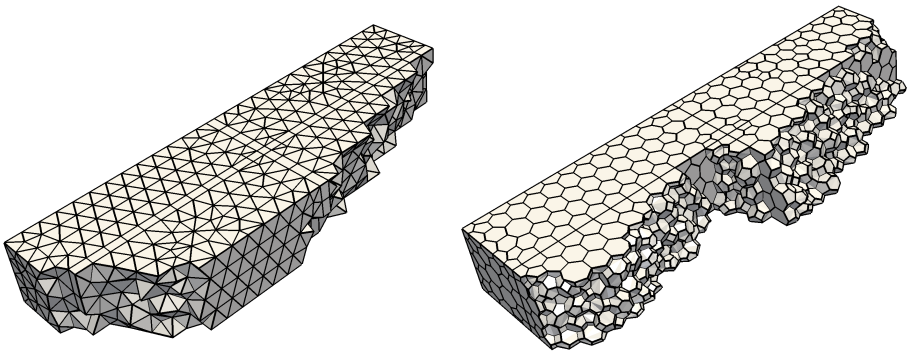

(b) Dual-cell boundary and well aligned grid (cross section), comprised of 1910 dual control volumes

Figure 14: Case-2: Primal and dual-cell interior boundaries and well aligned grids.

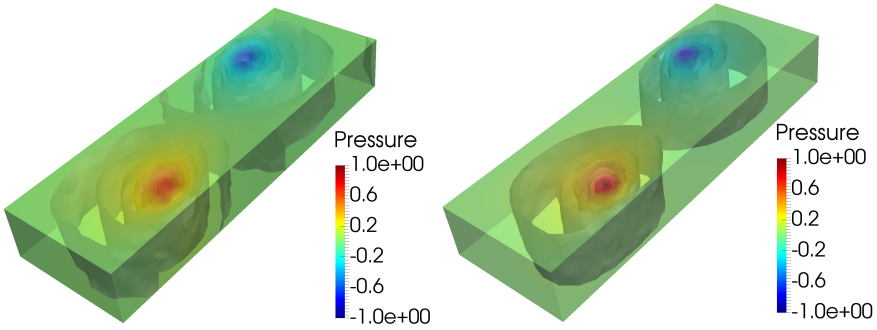

(a) Cell-Centered(left) versus vertex (right) centred TPFA solution

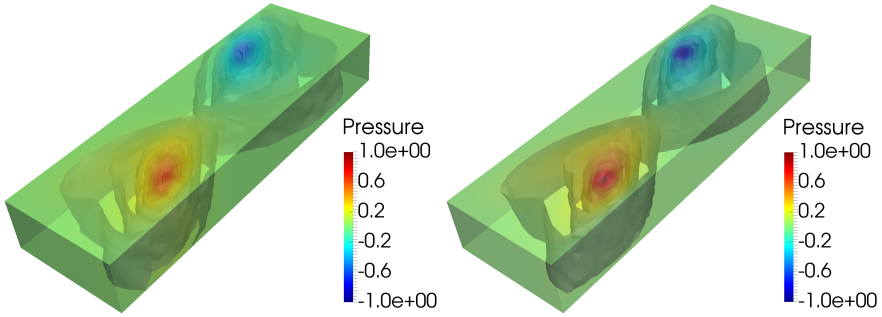

(b) Cell-Centered(left) versus vertex (right) centred CVD-MPFA-TPS solution

M-matrix statistics		Cell-Centred	Vertex-Centred
# of -ve diagonals		5	0
# of positive off-diagonal per row	L_∞	49.000	9.000
	$\bar{x}$	27.399	2.975
	L_2	5.405	2.082
max. positive off-diagonal relative to the diagonal per row	L_∞	2.910×10^{1}	9.605×10^{-1}
	$\bar{x}$	1.050×10^{-1}	7.653×10^{-2}
	L_2	1.099×10^{0}	3.768×10^{-1}

(c) Degree of M-matrix violation of cell-centered vs cell-vertex CVD-MPFA-TPS

Figure 15: Case-2a: Cell-centred versus vertex-centered numerical pressure solution obtained with TPFA and CVD-MPFA

5.2.2. Case 2b: Anisotropy ratio=50

Next we test a modified version of case 2a, where the anisotropy ratio is increased to 50, i.e., $k_{11}/k_{22} = 50$ and cross terms in z-direction are set by using $k_{13} = k_{31} = 5$. Similar to Case-2a, the orientation of permeability tensor is varied $\pm 30^{\circ}$ defining a strong discontinuous full tensor pressure field, e.g., see Equation 5. The pressure fields computed by employing cell-centered and vertex-centered TPFA are displayed in Figure 16a. The numerical pressure solutions computed by cell-centered and vertex-centered CVD-MPFA-TPS schemes are displayed in Figures 16b. While each TPFA solution has a LDMP with bounded numerical solution, however solution inconsistency is very pronounced when compared with the CVD-MPFA vertex-centered TPS pressure solution in Figure 16b(right), again the TPFA solution is unable to resolve the induced anisotropy of the pressure field. The cell-centred TPS result of Figure 16b(left), clearly shows strong spurious oscillations consistent with decoupling. On the other hand the vertex-centered TPS method is consistently found to be more robust with no visible spurious oscillations in the solution consistent with [21], see, Figure 16b(right). Again, the M-matrix violation comparison table 16c clearly shows that the cell-centered method has the worst violations which increases with (full-tensor) anisotropy ratio, suggesting that the unstructured vertex-centred method is quasi-positive and does not suffer from decoupling that is inherent in the cell-centered TPS formulation [27].

$$K = \begin{pmatrix} 37.750 & 21.218 & 5.000 \\ 21.218 & 13.250 & 0.000 \\ 5.000 & 0.000 & 13.250 \end{pmatrix} \tag{5}$$

5.3. Case-3: Multilateral well-trajectory and discontinuous full permeability tensor

This case is designed to simulate a pressure field, over a $\Omega = [0,1] \times [0,1] \times [0, 0.55]$ domain, involving a multilateral well path penetrating/intersecting a synthetic layer/fault defined by the plane $z = 0.20$, Figure 17, which bisects

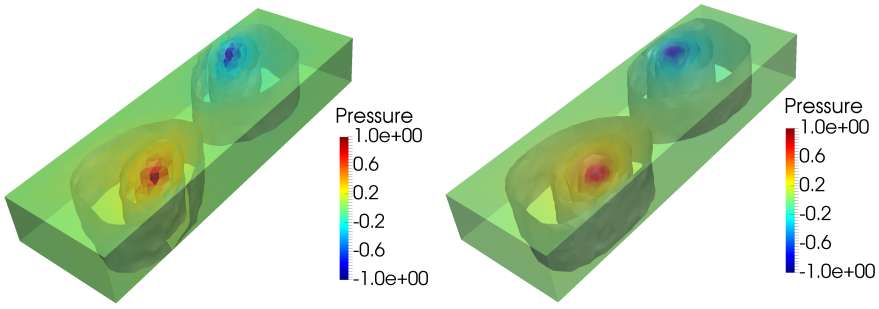

(a) Cell-Centered(left) versus vertex (right) centred TPFA solution

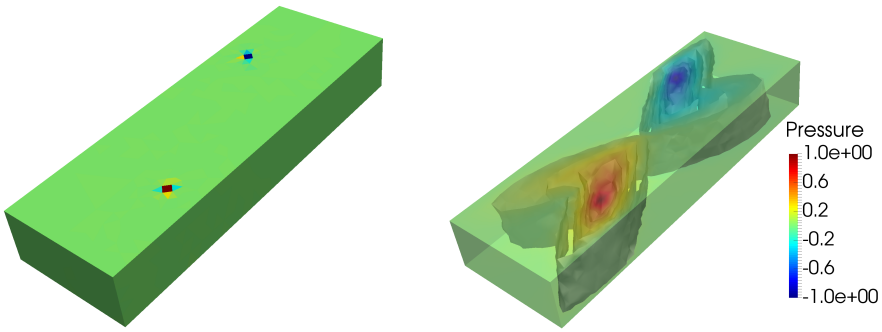

(b) Cell-Centered(left) versus vertex (right) centred CVD-MPFA-TPS solution

M-matrix statistics		Cell-Centred	Vertex-Centred
# of positive off-diagonal per row	L_∞	54.000	10.000
	$\bar{x}$	28.553	3.292
	L_2	5.504	2.151
max. positive off-diagonal relative to the diagonal per row	L_∞	2.013×10^3	1.203×10^0
	$\bar{x}$	1.678×10^0	9.794×10^{-2}
	L_2	2.393×10^1	4.116×10^{-1}

(c) Degree of M-matrix violation of cell-centered vs cell-vertex CVD-MPFA-TPS

Figure 16: Case-2b: Cell-centred versus vertex-centered numerical pressure solution obtained with TPFA and CVD-MPFA.

the domain into two sub-domains. In each sub-domain a piecewise constant permeability field is specified, which is discontinuous across the plane $z = 0.20$. The multilateral well-trajectory is considered as a geometrical object where imposed Dirichlet boundary conditions are prescribed with pressure $\phi = 1$. The system is closed with homogeneous Dirichlet boundary conditions specified with pressure $\phi = 0$ on the domain sides together with no-flow conditions prescribed at the top and bottom of the domain. This case requires grids which are both boundary and well-aligned. As described above, the generation of grids honouring geological features with respect to control volumes (BAG) involves entirely different strategies compared to those requiring control point alignment (WAG). This is further exacerbated, when these features appear while intersecting each other, since they meet conflicting requirements at the point of intersection. For such complex geometries the proposed feature based triangulation technique proves versatile. Details of the primal and dual grid generation for this case are presented in section 3. The resulting primal and dual-cell boundary and well-aligned meshes thus obtained are shown in Figures 17a and 17b respectively. The boundary and well-aligned grids generated are hybrids and comprised of tetrahedra (predominantly), prisms and hexahedra (required for halo) together with pyramids. Pyramids are used as transition elements from quad faces of halo cells to the rest of the mainly tetra mesh.

5.3.1. Case 3a: Discontinuous permeability tensor with anisotropy ratio=50

The first test involves an anisotropic ratio 50 : 1 in xy-plane, with respective orientations of ($\pm 30^\circ$) in the two sub-domains, leading to a discontinuous permeability field. A planar full-tensor is defined with $k_{13} = k_{31} = 5.00$, and $k_{33} = k_{22}$, in third dimension. In the lower sub-domain the permeability tensor is:

$$K = \begin{pmatrix} 37.75 & 21.22 & 5.00 \\ 21.22 & 13.25 & 0.00 \\ 5.00 & 0.00 & 13.25 \end{pmatrix} \tag{6}$$

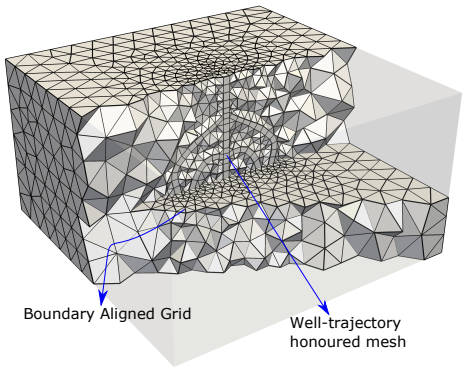

(a) Cross-section of primal-cell hybrid (23152 tets, 350 pyramids, 8 prisms, and 89 hexahedron) BAG employed for cell-centered formulation (23599 control volumes)

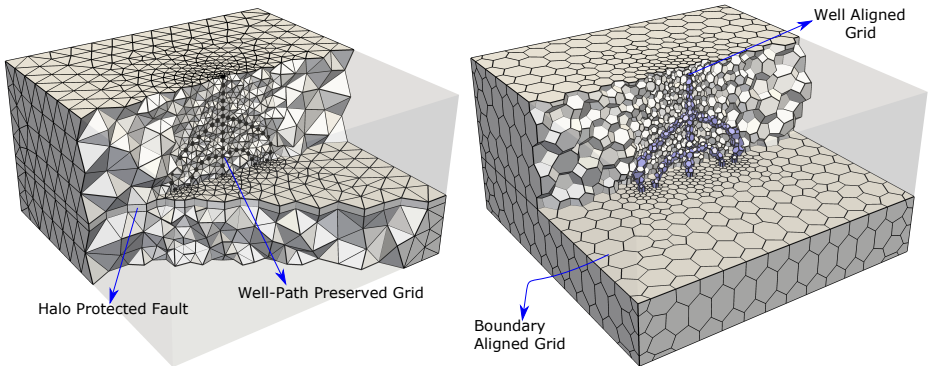

(b) Cross-section of prism-halo protected primal-cell (27982 tets, and 856 prisms) grid, used for vertex-centered formulation, also shown is dual-BAG derived from the halo protected primal-mesh (7146 control volumes)

Figure 17: Case-3: Boundary aligned grids:(a) primal cell-centered mesh and (b) vertex-centered mesh and dual-mesh with control-vols aligned with boundary.

whereas in the upper region ($0.20 < z \leq 0.55$) the permeability tensor has the same diagonals but negative off-diagonals with, $k_{12} = k_{21} = -21.22$ and $k_{13} = k_{31} = -5.00$. The numerical pressure solution computed by employing CVD-MPFA-TPS using cell-centered and vertex-centered methods is displayed in Figures 18a and 18b respectively. As in the previous case we note that both methods violate the M-matrix conditions, the most severe violations by far (by 12 orders of magnitude in maximum positive off-diagonal) occurring with the cell-centred method again suggesting by comparison that the vertex centred method is quasi-positive [20]. In this case both the cell-centered and vertex-centered methods yield well resolved pressure fields, with no visible spurious non-physical oscillations.

5.3.2. Case 3b: Discontinuous full permeability tensor with anisotropy ratio=500

Next an analogous case is considered with an increased anisotropy ratio of $500:1$ in xy plane, and same ($\pm 30^{\circ}$) orientations in the respective sub-domains, defining a much larger jump in discontinuous permeability field across $z = 0.2$. A planar full-tensor is defined with $k_{13} = k_{31} = 15.00$, and $k_{33} = k_{22}$, in third dimension. In the lower sub-domain the permeability tensor is:

$$K = \begin{pmatrix} 375.25 & 216.07 & 15.00 \\ 216.07 & 125.75 & 0.00 \\ 15.00 & 0.00 & 125.75 \end{pmatrix} \tag{7}$$

whereas in the upper region ($0.20 < z \leq 0.55$) the permeability tensor has negative off-diagonals, i.e. $k_{12} = k_{21} = -216.07$ and $k_{13} = k_{31} = -15.00$. The problem poses serious challenges to the numerical schemes, which are mainly due to the large anisotropic ratio and local grid orientation effects. Figure 19 shows the numerical pressure fields obtained by employing both the cell-centered and vertex-centered TPS schemes. The cell-centered TPS formulation strongly violates the M-matrix conditions and introduces non-physical oscillations consistent with decoupling [20], e.g., see Figure 19a, whereas vertex-centered TPS Figure 19b, yields a well resolved solution that is free of any visible spurious oscillations consistent with the decoupling analysis of [21]. We note that as

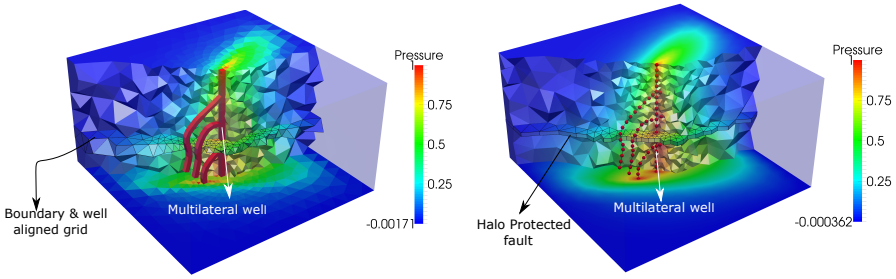

(a) Cell-Centred CVD-MPFA-TPS numerical solution

(b) Vertex-Centred CVD-MPFA-TPS numerical solution

M-matrix statistics		Cell-Centred	Vertex-Centred
# of positive off-diagonal per row	L_∞	48.00	10.00
	$\bar{x}$	25.99	4.15
	L_2	5.247	2.247
max. positive off-diagonal relative to the diagonal per row	L_∞	3.270×10^{13}	8.656×10^{-1}
	$\bar{x}$	1.648×10^{9}	9.527×10^{-2}
	L_2	5.333×10^{6}	3.591×10^{-1}

(c) Degree of M-matrix violation of cell-centered vs cell-vertex CVD-MPFA-TPS

Figure 18: Case-3a: Cell-centred versus vertex-centered CVD-MPFA-TPS numerical pressure solutions, contours displayed in cross-section.

in the previous case, while both methods violate the M-matrix conditions, by far the most severe violations (now by 13 orders of magnitude) occur with the cell-centred method, with a further order of magnitude difference in this case, again suggesting by comparison that the vertex centred method is quasi-positive [20]. We conclude that the unstructured vertex-centered TPS formulation does not suffer from decoupling that is inherent in the cell-centered TPS formulation [27].

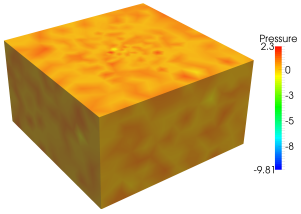

(a) Cell-Centred TPS numerical solution with non-physical oscillations

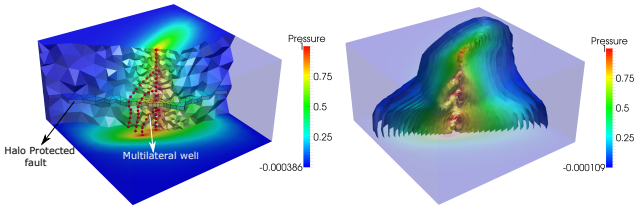

(b) Vertex-Centred TPS numerical solution

M-matrix statistics		Cell-Centred	Vertex-Centred
# of positive off-diagonal per row	L_∞	49.00	11.00
	$\bar{x}$	25.06	4.256
	L_2	5.161	2.276
max. positive off-diagonal relative to the diagonal per row	L_∞	1.115×10^{14}	9.093×10^{-1}
	$\bar{x}$	4.725×10^{9}	1.092×10^{-1}
	L_2	1.056×10^{7}	3.976×10^{-1}

(c) Degree of M-matrix violation of cell-centered vs cell-vertex TPS

Figure 19: Case-3b: Cell-centred versus vertex-centered TPS numerical pressure solutions, contours displayed in cross-section

.

6. Summary of Grid Generation and CVD-MPFA Comparison

We note that the primal cell-centered and dual cell-vertex CVD-MPFA formulations are essentially analogous on structured grids. However on general unstructured grids discretization compatibility requirements add additional challenges to grid generation that are addressed in this work, which for the first time makes both the primal and dual formulations suitable for practical application. We summarize key steps in the novel grid generation process and then list key observations regarding TPFA and cell-centered and dual cell-vertex CVD-MPFA formulations on unstructured grids.

6.1. Grid Generation Summary

The key novel components of the geological feature based grid generation methods presented are:

- Unique work flow for generating feature based cell-centered and vertex-centered grids is presented
- *Protection spheres:* When generating primal-cell boundary aligned and dual-cell well-aligned meshes, geological features are honoured in the empty-mesh and are protected by enclosing them with protection spheres, which are diametric, equatorial and/or circumspheres according to simplex type i.e. (edge/face) and emptiness of the associated protection sphere.
- *Cell-centred Primal Mesh Halo construction:* For primal-cell halo well-aligned grids, halo construction is performed by sweeping a polygon along the well-trajectory analogous to the advancing front method.
- *Vertex-centred Dual Mesh Halo construction:* Geological feature boundaries are protected by embedding their surfaces in prismatic halos, such that halo medial surfaces lie on the boundary surfaces, which is achieved by splitting each surface mesh point into an edge, followed by triangulation that yields tets, pyramids and/or prisms.

- *Novel technique for suppressing Steiner points:* A novel technique for suppressing additional connectivity points, i.e. Steiner points is proposed. An empty-mesh is primarily comprised of tetra. By deleting repeated interior faces of elements sharing the *Steiner* point, a star-shaped polyhedron is constructed, and the Steiner point is suppressed by projecting it in a direction normal to the intersected face/edge inside the star-shaped polyhedron. A set of new elements(tets) is then constructed by joining each face(tri) of the star-shaped polyhedron to the projected Steiner point.

- *A novel technique for constructing pyramids as transition elements:* The empty-mesh is comprised of tetrahedra and after recovery of halo quad-faces, pyramids are constructed as transition elements in the unstructured mesh via a star-shaped polyhedron construction and point insertion procedure, thus protecting halo quad-faces, with tetrahedra connected to the triangular faces.

6.2. CVD-MPFA Discretization Summary

- TPFA cell-centered and vertex-centered formulations are inconsistent on non K-orthogonal grids.

- Cell-vertex dual-mesh simulation requires much less computational time compared to the corresponding cell-centered primal grid formulation. This is because the cell-centered formulation involves between approximately 4 and 5 times the number of degrees of freedom compared to the cell-vertex formulation, when using the same primal unstructured (tetrahedra) grid. The cell-vertex method is thus computationally more efficient for a given tetrahedral mesh.

- Cell-vertex CVD-MPFA formulations with TPS are computationally more robust than their cell-centered counter part formulations on unstructured grids, even with between a quarter to one fifth of the number of degrees of freedom, the cell-vertex formulation yields consistent well resolved solutions consistent with [21]. Such resolution is not always achieved by

the cell-centered counter part TPS formulation which can yield highly oscillatory decoupled pressure fields (in particular when applied to e.g. source/sink problems with strong full-tensor fields) consistent with [27], even though the cell-centered method uses more degrees of freedom.

- Tables showing a measure of M-matrix violation for challenging cases verifies the robustness of the cell-vertex methods with relatively small M-matrix violation compared to the cell-centered methods which have strong violation.

- Cell vertex CVD-MPFA schemes are more compact than their cell-centered counterparts on unstructured grids resulting in globally assembled matrices with smaller bandwidth.

- The dual-control-volumes of the compact cell-vertex CVD-MPFA formulations on unstructured grids have more facets than primal cells and consequently involve more sub-face fluxes per control volume, compared to the cell-centered formulation, which may contribute to the observed improvement in resolution.

7. Conclusions

Novel methods of grid generation are presented that honour geological features both with respect to primal and dual cells. The CVD-MPFA formulation overcomes the consistency limitation of the standard TPFA scheme used routinely in reservoir simulation. However crucially for general application, CVD-MPFA control-volume faces must be aligned with key feature surfaces when generating the mesh. This paper presents boundary aligned unstructured grid generation methods that satisfy these key constraints for both cell-centred and vertex centred CVD-MPFA formulations in three-dimensions.

The development of halos and protection spheres surrounding key feature boundary surfaces are central to the boundary aligned grid generation methods presented. The resulting grids are predominantly tetrahedral and Delaunay

where the empty circumsphere property is ensured. When halos are required (for discretization compatibility), the method naturally generates transition grids comprised of combinations of pyramids, prisms, tetrahedra and/or hexahedra (polygonal prisms) to handle geological features with boundary alignment.

This development has also enabled the first detailed 3-D comparison to be made between the primal (cell-centred) and dual-cell (vertex centred) CVD-MPFA formulations using comparable primal meshes, and major computational advantages of the dual-cell formulation are identified: i) computational efficiency due to the number of vertices being a fraction of the number of cells for a given unstructured grid. ii) compact support with significantly reduced bandwidth and iii) prevention of decoupled modes that cause spurious oscillations on the essentially tetra meshes.

Future work will include using the latest developments to test more challenging geometries resulting from classical reservoir features (highly distorted faults, fractures, pinchouts, variable layered systems and intersections, with various surface models and representations including non-uniform rational basis splines [36]) together with multilateral wells. The algorithms presented are quite general and we anticipate that any modifications for handling more distorted features is relatively straightforward, however much testing needs to be conducted. Further extensions include coupling with unstructured multiscale methods (which involve a number of strategies [66, 71, 15]) to develop general unstructured grid multiscale methods in 3-D, extension to multiphase flow and field scale applications.

Acknowledgements

We thank the referees for their constructive comments which have helped us to improve the manuscript.

References

[1] I. Aavatsmark, T. Barkve, O. Boe, and M. Mannseth [1998] Discretization on Unstructured Grids for Inhomogeneous, Anisotropic Media. Part I: Derivation of the Methods. *SIAM Journal on Scientific Computing* 19: 1700-1716.

[2] I. Aavatsmark [2002] An Introduction to Multipoint Flux Approximations for Quadrilateral Grids. *Computational Geosciences* 6(3),405–432.

[3] R. Ahmed, M.G. Edwards, S. Lamine, B.A.H. Huisman and M. Pal [2015] Control Volume Distributed Multi-Point Flux Approximation coupled with a lower-dimensional fracture model. *J. Comput. Phys* vol 284 pp 462-489 March 2015.

[4] R. Ahmed, M.G. Edwards, S. Lamine, B.A.H. Huisman and M. Pal [2015] Three-dimensional Control Volume Distributed Multi-Point Flux Approximation coupled with a lower-dimensional surface fracture model. *J. Comput. Phys* vol 303 pp 470-497 Dec 2015.

[5] V. Artus, D. Fructus, and Olivier Houzé [2017] Simulation of Deviated Wells Using 3D Unstructured Grids of Flexible Resolution. *SPE RSC, Texas, USA (SPE-182645-MS)*, 20-22 February 2017.

[6] K. Aziz, and A. Settari [1972] Use of Irregular Grid in Reservoir Simulation. *SPE Journal*, 12, 103 114, 1972.

[7] D. Arnold [1990] Mixed finite element methods for elliptic problems. *Comput. Meth. Appl. Mech. Engrg*, 281-300.

[8] T. Barth [1994] Aspects of Unstructured Grids and Finite Volume Solvers for the Euler and Navier-Stokes Equations. *Computational Fluid Dynamics No. 1994–04 in Lecture Series, von Karman Institute for Fluid Dynamics*

[9] R.L. Berge, Ø.S. Klemetsdal, and K. Lie [2019] Unstructured Voronoi grids conforming to lower dimensional objects. *Comput Geosci 23, 169–188, doi:10.1007/s10596-018-9790-0*

[10] F. Brezzi and M. Fortin [1991] Mixed and Hybrid Finite Element Methods. *Springer-Verlag.*

[11] Y. Chen, B.T. Mallison, & L.J. Durlofsky [2008] Nonlinear two-point flux approximation for modeling full-tensor effects in subsurface flow simulations. *Comput Geosci* 12, 317335, doi:10.1007/s10596-007-9067-5.

[12] H. Chen, J. Kou, S. Sun, and T. Zhang [2019] Fully mass-conservative IMPES schemes for incompressible two-phase flow in porous media. *Computer Methods in Applied Mechanics and Engineering*, 350, 641–663.

[13] D. Contreras, and N. Hitschfeld-Kahler [2014] Generation of Polyhedral Delaunay Meshes. *Procedia Engineering*, 82, 291-300.

[14] L. Chew [1989] Constrained Delaunay triangulations. *Algorithmica*, 4, 97-108, 1989.

[15] A.C.R.deSouza, L.M.C. Barbosa, F.R.L. Contreras, P.R.Lyra, D.deCarvalho [2020] A Multiscale Control Volume framework using the Multiscale Restriction Smooth Basis and a non-orthodox Multi-Point Flux Approximation for the simulation of two-phase flows on truly unstructured grids *J. Pet. Sci and Eng Vol 188, May 2020.*

[16] M.G. Edwards, and C.F. Rogers [1998] Finite volume discretization with imposed flux continuity for the general tensor pressure equation. *Computational Geosciences*, 2, 259–290.

[17] M.G. Edwards [2006] Higher-resolution hyperbolic-coupled-elliptic flux-continuous CVD schemes on structured and unstructured grids in 3-D. *Int. J. Numer. Meth. Fluids*, 51, 10791095.

[18] M.G. Edwards, and H. Zheng [2010] Double-families of quasi-positive Darcy-flux approximations with highly anisotropic tensors on structured and unstructured grids. *Journal of Computational Physics*, 229, 594–625.

[19] M.G. Edwards, and H. Zheng [2008] A quasi-positive family of continuous Darcy-flux finite-volume schemes with full pressure support. *Journal of Computational Physics*, 227, 9333–9364.

[20] M.G. Edwards, and H. Zheng, H. [2011] Quasi M-Matrix Multifamily Continuous Darcy-Flux Approximations with Full Pressure Support on Structured and Unstructured Grids in Three Dimensions. *SIAM Journal on Scientific Computing*, 33, 455-487.

[21] M.G. Edwards, and H. Zheng [2011] Quasi-Positive Anisotropic Darcy-Flux Finite-volume Approximation for General Grids and MPFA Decoupling Analysis. *Reservoir simulation symposium* SPE, 2011.

[22] B. Diskin, J. Thomas, E. Nielsen, J. White, and H. Nishikawa [2009] Comparison of Node-Centered and Cell-Centered Unstructured Finite-Volume Discretizations. *Part I: Viscous Fluxes.*

[23] P. Frey, and P. George [2008] Surface Meshing and Re-meshing. *Mesh Generation: Application to Finite Elements (Inbook)*, ISTE Ltd and John Wiley & Sons, Ltd, 491-523.

[24] P. Forsyth [1990] A control-volume finite element method for local mesh refinement in thermal reservoir simulation. *SPE Reservoir Engineering*, SPE-18415-PA, November 1990.

[25] S. Fortune [1997]. In: J.E. Goodman, and J. O'Rourke (Eds.) *Voronoi diagrams and Delaunay triangulations – Handbook of discrete and computational geometry*, 377–388.

[26] H.A. Friis, M.G.Edwards, and J. Mykkeltveit [2008] Symmetric Positive Definite Flux-Continuous Full-Tensor Finite-Volume Schemes on Unstruc-

tured Cell-Centered Triangular Grids. *SIAM Journal on Scientific Computing*, 31, 1192–1220.

[27] H.A. Friis, and M.G. Edwards [2011] Family of MPFA finite-volume schemes with full pressure support for the general tensor pressure equation on cell-centered triangular grids. em Journal of Computational Physics , 230(1), 205–231.

[28] X. Feng, and X. Liao [2020] Study on Well Spacing Optimization in a Tight Sandstone Gas Reservoir Based on Dynamic Analysis. *ACS omega*, 5(7), 37553762,

[29] P. George, H. Borouchaki, P. Frey, and P. Laug, and E. Saltel [2004] Mesh Generation and Mesh Adaptivity: Theory and Techniques Encyclopedia of Computational Mechanics, John Wiley & Sons, Ltd.

[30] L. Guibas, and J. Stolfi [1985] Primitives for the manipulation of general subdivisions and the computation of Voronoi. *ACM Trans. Graph.*, 4(2), 74–123.

[31] P.J. Green, and R. Sibson [1978] Computing Dirichlet Tessellations in the Plane. *The Computer Journal*, 21(2), 168–173.

[32] P.L. George, H. Borouchaki [1998] In: HERMES(Ed) *Delaunay Triangulation – Delaunay Triangulation and Meshing Applications to Finite Elements*, 37,238.

[33] P. George, H. Borouchaki, and E. Saltel [2003] Ultimate robustness in meshing an arbitrary polyhedron. *Int. J. Numer. Methods Eng.*, 58, 1061-1089.

[34] O. Hassan, E. Probert, K. Morgan, and N.P. Weatherill [2000] Unsteady flow simulation using unstructured meshes. *Computer Methods in Applied Mechanics and Engineering*, 189, 1247-1275.

[35] H. Hægland, A. Assteerawatt, H. Dahle, G. Eigestad, and R. Helmig [2009] Comparison of cell- and vertex-centered discretization methods for flow in a two-dimensional discrete-fracture-matrix system. *Advances in Water Resources*, 32, 1740-1755.

[36] TJR Hughes, JA Cottrell, Y. Bazilevs [2005] Isogeometric analysis: CAD finite elements, NURBS, exact geometry and mesh refinement. *Comput Methods Appl Mech Eng* 194(3941):41354195.

[37] Sazonov I., Wang D., Hassan O., Morgan K., and Weatherill N.P. [2006] A stitching method for the generation of unstructured meshes for use with co-volume solution techniques. *Computer Methods in Applied Mechanics and Engineering*, 195(13-16),1826–1845, 2006.

[38] Y. Kallinderis, A. Khawaja, and H. McMorris [1996] Hybrid prismatic/tetrahedral grid generation for complex 3-D geometries.*AIAA Journal*, 1996, 34, 291-298.

[39] M. Karimi-Fard [2004] Growing Region Technique Applied to Grid Generation of Complex Fractured Porous Media. *ECMOR IX- 9th European Conference on the Mathematics of Oil Recovery*, 2004.

[40] M. Karimi-Fard [2008] Grid Optimization to Improve Orthogonality of Two-point Flux Approximation for Unstructured 3D Fractured Reservoirs. *ECMOR-XI conference*, doi=10.3997/2214-4609.20146380.

[41] M. Karimi-Fard, and L.J. Durlofsky [2016] A General Gridding, Discretization, and Coarsening Methodology for Modeling Flow in Porous Formations With Discrete Geological Features. *Advances in Water Resources 96: 354372*

[42] E. Keilegavlen, and I. Aavatsmark [2011] Monotonicity for MPFA methods on triangular grids. *Computational Geosciences*, 15, 3-16.

[43] Ø.S. Klemetsdal, R.L. Berge, K.A. Lie, H.M.Nilsen, and O. Møyner [2017]. Unstructured Gridding and Consistent Discretizations for Reservoirs with

Faults and Complex Wells. *SPE RSC, Texas, USA (SPE-182666-MS)*, 20-22 February 2017.

[44] I. Kocabas, and F. Maier [2013] Analytical and Numerical Modeling of Tracer Flow in Oil Reservoirs Containing High Permeability Streaks. *Middle East Oil and Gas Show and Conference (SPE)*.

[45] D.T. Lee, and B.J. Schachter [1980] Two algorithms for constructing a Delaunay triangulation.*International Journal of Computer & Information Sciences*, 9(3), 219–242.

[46] R. Löner, and P. Parikh [1988] Three dimensional grid generation by advancing front method. *International Journal for Numerical Methods in Fluids*, 8, 1135–1149.

[47] S. Lee, L. Durlofsky, M. Lough, and W. Chen [1998] Finite difference simulation of geologically complex reservoirs with tensor permeabilities. *SPE Reservoir Evaluation & Engineering*, 1, 567-574.

[48] P. Laug, and H. Borouchaki [2011] High quality geometric meshing of CAD surfaces. *Proceedings of the 20th international meshing roundtable*, W.R. Quadros (Ed.).

[49] P.Laug, and H. Borouchaki [2004] Curve linearization and discretization for meshing composite parametric surfaces. *Commun. Numer. Meth. Engng*, 20, 869876, 2004.

[50] Y. Liu, S. Lo, Z.Q.Guan, and H.W. Zhang [2014] Boundary recovery for 3D Delaunay triangulation. *Finite Elements in Analysis and Design*, 84, 32-43, 2014.

[51] C. Lawson [1986] Properties of n-dimensional triangulations. *Computer Aided Geometric Design*, 3, 231-246.

[52] K. Lipnikov, G. Manzini, and M. Shashkov [2014] Mimetic Finite Difference Method. *J. Comput. Phys.*, 257, 1163–1227.

[53] K. Lipnikov, D. Svyatskiy, and Y. Vassilevski [2012] Minimal stencil finite volume scheme with the discrete maximum principle. *Russ. J. Numer. Anal. Math. Modelling*, 27(4), 369–385.

[54] B. Mallison, C. Sword, T. Viard, W. Milliken, A. Cheng [2014] Unstructured Cut-Cell Grids for Modeling Complex Reservoirs. *SPEJ vol 19, Issue 02, doi.org/10.2118/163642-PA*

[55] S. Manzoor, M.G. Edwards, A.H. Dogru, and T.M. Shaalan [2015] Boundary Aligned Grid Generation in Three Dimensions and CVD-MPFA Discretization. *SPE Reservoir Simulation Symposium*, 23-25 February.

[56] S. Manzoor, M.G. Edwards, A.H. Dogru, and T.M. Al-Shaalan [2016] 3D Geological Feature Honored Cell-centered and Vertex-centered Unstructured Grid Generation, and CVD-MPFA Performance. *ECMOR XV - 15th European Conference on the Mathematics of Oil Recovery.*

[57] S. Manzoor, M.G. Edwards, A.H. Dogru, T.M. Shaalan [2018] Interior boundary-aligned unstructured grid generation and cell-centered versus vertex-centered CVD-MPFA performance. *Computational Geosciences*, 22(1), 195230, 2018.

[58] S. Manzoor, M.G. Edwards, and A.H. Dogru [2018b] Acute Boundary Aligned Unstructured Grid Generation And Consistent Flux Approximations.*ECMOR XVI - 16th European Conference on the Mathematics of Oil Recovery*, 2018.

[59] S. Manzoor, M.G. Edwards, and A.H. Dogru [2019] Three-Dimensional Geological Boundary Aligned Unstructured Grid Generation, and CVD-MPFA Flow Computation. *SPE 193874, Reservoir Simulation Conference, Galveston Texas USA*, 10-11th April 2019

[60] S.Manzoor, M.G.Edwards, A.H. Dogru [2019]. Quasi-K-Orthogonal Grid Generation. *Society of Petroleum Engineers*, March 29, 2019. doi:10.2118/193927-MS.

[61] S. Matthai, A.A. Mezentsev, and M. Belayneh [2007] Finite element-node-centered finite-volume two-phase-flow experiments with fractured rock represented by unstructured hybrid-element meshes.*SPE Reservoir Evaluation & Engineering*, 10(6), 740-756.

[62] D. Marcum, and K. Gaither [1997] Solution Adaptive Unstructured Grid Generation Using Pseudo-Pattern Recognition Techniques. *AIAA 13th Computational Fluid Dynamics Conference*, 1997.

[63] D.L. Marcum, and N.P. Weatherill [1995] Unstructured grid generation using iterative point insertion and local reconnection. *AIAA Journal*, 33, 1619–1625.

[64] D.J. Mavriplis [1995] An Advancing Front Delaunay Triangulation Algorithm Designed for Robustness. *Journal of Computational Physics*, 117, 90–101.

[65] M. Mlacnik, and L. Durlofsky [2006] Unstructured Grid Optimization for Improved Monotonicity of Discrete Solutions of Elliptic Equations with Highly Anisotropic Coefficients. *J. Comput. Phys.*, 216, 337-361.

[66] O.Moyner, K.-A. Lie [2015] A multiscale restriction-smoothed basis method for high contrast porous media represented on unstructured grids *J. Comput. Phys.*, 304 (2015), pp. 46-71.

[67] J.D. Müller, P.L. Roe, and H. Deconinck [1993] A frontal approach for internal node generation in Delaunay triangulations. *International Journal for Numerical Methods in Fluids*, 17(3), 241-255.

[68] H.M. Nilsen, J.R. Natvig, K-A. Lie [2012] Accurate modeling of faults by multipoint, mimetic, and mixed methods. *SPE journal*, 17(02).

[69] M. Pal, and M.G. Edwards [2010] q-Families of CVD(MPFA) Schemes on General Elements: Numerical Convergence and the Maximum Principle. *Archives of Computational Methods in Engineering*, 17, 137-189.

[70] M. Pal, and M.G. Edwards [2012] A family of multi-point flux approximation schemes for general element types in two and three dimensions with convergence performance. *International Journal for Numerical Methods in Fluids* 69(11), 1797-1817.

[71] E. Parramore, M.G. Edwards, M. Pal, and S. Lamine [2016] Multiscale Finite-Volume CVD-MPFA Formulations on Structured and Unstructured Grids *SIAM Multiscale Model. Simul., 14(2), 559594. 2016.*

[72] J.O'. Rourke [1987] Art Gallery Theorems and Algorithms. *Three Dimensions and Miscellany*, Oxford University Press, 253-254. Editors: J.E. Hopcroft, G.D. Plotkin, J. Schwartz, D. Scott, and J. Vuillemin.

[73] S. Rebay [1993] Efficient Unstructured Mesh Generation by Means of Delaunay Triangulation and Bowyer-Watson Algorithm.*Journal of Computational Physics*, 106(1), pp. 125138.

[74] T.Russell, and M. Wheeler [1984] The Mathematics of Reservoir Simulation Finite element and finite difference methods for continuous flows in porous media. *Frontiers in Applied Mathematics*, SIAM, 35-106.

[75] P. Samier, and R. Masson [2017]. Implementation of a Vertex-Centered Method Inside an Industrial Reservoir Simulator: Practical Issues and Comprehensive Comparison With Corner-Point Grids and Perpendicular-Bisector-Grid Models on a Field Case. *SPEJ vol 22, Issue 02, doi.org/10.2118/173309-PA*

[76] P Salinas, D Pavlidis, Z Xie, H Osman, CC Pain, MD Jackson [2018] A discontinuous control volume finite element method for multi-phase flow in heterogeneous porous media. *Journal of Computational Physics*, 352, 602-614, 2018.

[77] P. Su, and R.L. Scot [1997] A comparison of sequential Delaunay triangulation algorithms. *Computational Geometry–11th ACM Symposium on Computational Geometry*, 7(5-6), 361–385.

[78] S. Sloan, and G. Houlsby [1984] An implementation of Watson's algorithm for computing 2-dimensional delaunay triangulations *Advances in Engineering Software*, 6, 192-197.

[79] S.A. Sloan [1993] Fast algorithm for generating constrained delaunay triangulations.*Computers & Structures*, 47, 441-450.

[80] M. Sahimi, R. Darvishi, M. Haghighi, and M. Rasaei [2010] Upscaled Unstructured Computational Grids for Efficient Simulation of Flow in Fractured Porous Media. *Transport in Porous Media*, 83, 195-218.

[81] I. Sazonov, and P. Nithiarasu [2012] Semi-automatic surface and volume mesh generation for subject-specific biomedical geometries. *International Journal for Numerical Methods in Biomedical Engineering*, 28, 133-157.

[82] J.F. Thompson, and N.P. Weatherill [1998], Chapter: Fundamental Concepts and Approaches. In *Handbook of Grid Generation*; Thompson, J.F., Soni, B, K. and Weatherill, N.P.(Eds.).

[83] U. Tremel, F. Deister, O. Hassan, and N.P. Weatherill [2004] Automatic unstructured surface mesh generation for complex configurations. *International Journal for Numerical Methods in Fluids*, 45, 341-364, 2004.

[84] S.K. Verma [1996] Flexible grids for reservoir simulation. *PhD Thesis*, Stanford University.

[85] N.P. Weatherill [1992] Delaunay triangulation in computational fluid dynamics.*Computers & Mathematics with Applications*, 24, 129-150.

[86] N.P. Weatherill, and O. Hassan [1994] Efficient three-dimensional Delaunay triangulation with automatic point creation and imposed boundary constraints.*International Journal for Numerical Methods in Engineering*, 37, 2005-2039.

[87] D.F. Watson [1981] Computing the n-dimensional Delaunay tessellation with application to Voronoi polytopes. *The Computer Journal*, 24(2), 167–172.

[88] M.F. Wheeler and I. Yotov [2006] A multipoint flux mixed finite element method. *SIAM J. Numer. Anal.* , 44:5 2082-2106.

Appendices

A. Delaunay admissible simplexes and protection-spheres

A simplical mesh is comprised of points (0-D simplexes), edges (1-D simplexes), triangles (2-D simplexes), and tetrahedra(3-D simplexes). In D dimensions for a Delaunay triangulation, a $D-i$ $(\forall i = 1, D-1)$ simplex whose smallest sphere is empty, exists in the mesh. The smallest sphere encompassing an edge (segment) is the sphere containing the edge as its diameter, i.e., diametric sphere. For a triangle, the smallest sphere contains the triangle as its equatorial plane, and is the equatorial sphere. In three dimensional Delaunay triangulation, for an edge whose smallest sphere is not empty to exist, a triangle must be formed by joining the edge at hand to the point being nearest to the edge, contained in its diametric sphere. If the smallest sphere of a triangle (existing in a Delaunay mesh) is not empty then there must be a tetra with connectivity defined by joining vertices of the triangle to the point which is contained in its equatorial sphere and is the nearest to the triangle (plane). In a Delaunay triangulation the circumsphere of a tetrahedron is always empty[51, 32]. The Delaunay admissibility of the simplexes constituting a Delaunay mesh, is summarized in the following theorem:

Theorem 1. *In D dimensions, for a $D-i$ simplex $\forall i = 1, D-1$ to be part of a Delaunay triangulation either its smallest sphere is empty or there exist a $(D-i)+j$ simplex $\forall j = 1, i$ with empty smallest sphere.*

B. Halos enclosing well-paths (description and implementation)

Consider $\vec{e}_1$ and $\vec{e}_2$ as two edge vectors sharing a summit-node labeled p_2 defining a pyramid $(b_1 b_2 b_3 b_4 p_2)$, as shown in Figure 20a. The base of the pyra-

mid is a quad defined by points, $b_i \ \forall i = 1:4$, the translation of the base of the pyramid is given by:

$$t_i = b_i + \vec{e}_1; \quad \forall i = 1:4$$

where t_i represents points of the swept quad, e.g., see Figure 20a. In case well-trajectories are vertical or nearly vertical, the above translation of a sweeping polygon along the well-paths leads to formation of a quality hexahedron enclosing the well-paths. Nevertheless this simple translation when used to construct a halo around curved well-paths, is found to yield low quality distorted pinched out hexahedra. This is because each interior point (and associated sweep polygon) of a well-trajectory is associated with two edges (hence two hexahedrons). To correct the position of a translated polygon we project it onto the plane passing through summit-node (p_2) defined with normal $\vec{n}_p$ given by:

$$\vec{n}_p = \frac{\vec{e}_1 + \vec{e}_2}{||\vec{e}_1 + \vec{e}_2||} \tag{8}$$

i.e. to the bisection plane of edge $\vec{e}_1$ and $\vec{e}_2$. While correcting the position of the swept polygon, induced by the projection, changes in the dimension(size) of the swept polygon occurs, viewed with respect to the reference sweeping polygon. To delimit this local size and/or shape change of the swept polygon, an additional step involving size correction is used. The size correction is performed by ensuring that the distance of corners(t_i) of the swept polygon with respect to summit-node(p_2), matches those of the reference polygon in a 1-1 correspondence, i.e. $||p_2 t_i|| = ||p_1 b_i||$, where p_2 is the summit-node and p_1 is the centroid of the base(b_i), e.g., see Figure 20c. At each summit-node a new(swept) face is constructed first by translating its base, this is followed by projection and finally size correction. By joining the newly constructed quad face at the summit-node to the base of the pyramid a hexahedron, together with a pyramid obtained by joining the quad face at the summit-node to the following point of edge $\vec{e}_2$, (to p_3 in Figure 20) is constructed. The size correction step is found to be useful for highly curved well-trajectories and/or multilateral well-paths described in section 3.1.

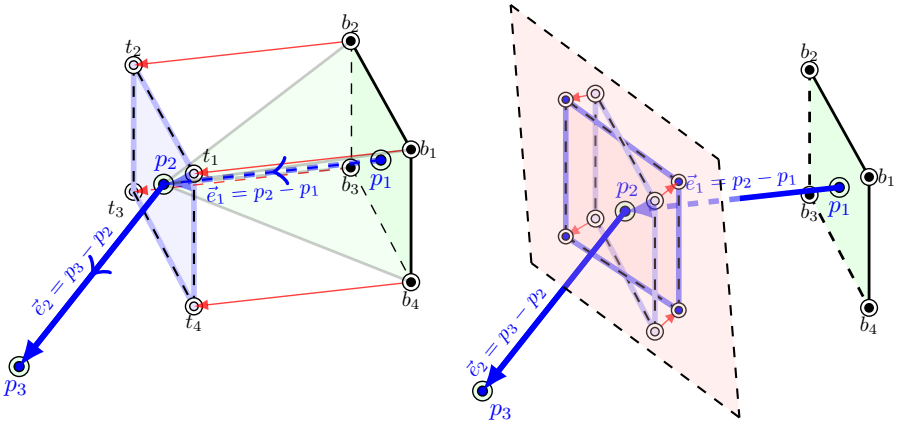

(a) Translation of base ($b_1b_2b_3b_4$) of pyramid ($b_1b_2b_3b_4p_2$) along vector $\vec{e}_1$

(b) Projection of the swept face to the bisection plane of $\vec{e}_1$ and $\vec{e}_2$

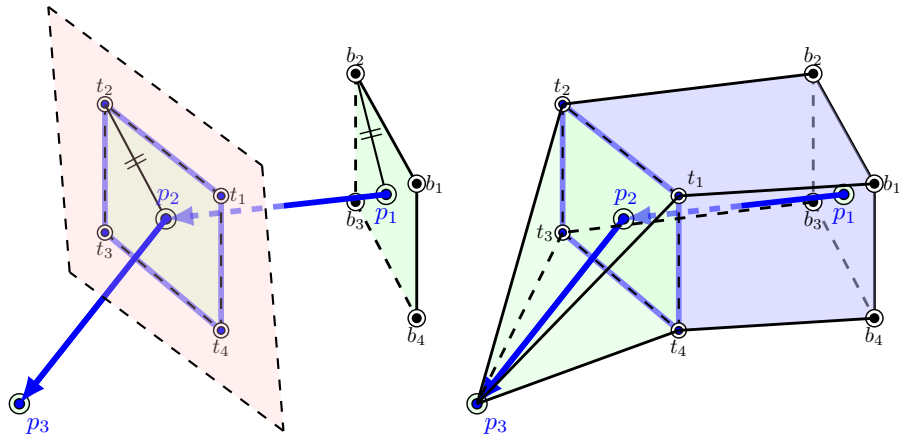

(c) Size corection, i.e. $|p_2t_i| = |p_1b_i|$

(d) Propagate spear constructing hexahedron 1-1

Figure 20: Procedure to sweep polygon along a well-trajectory

C. Halos enclosing geological objects (re-meshing SSP)

When re-meshing a star-shaped polyhedron(SSP) with respect to an edge $(p\bar{}q)$, one of three possible cases occurs, as displayed in Figure 21, and detailed below:

- *Case-1 (edge SSP):* This is the simplest case, where the point p to be split is shared by the surface-mesh triangles alone, and the associated star-shaped polyhedron (SSP) reduces to a star-shaped polygon comprising of edges (Figure 21a). First we split point p, by pushing it in upward and downward directions yielding an edge $(p\bar{}q)$, then joining each edge of the star-shaped polygon to the edge $(p\bar{}q)$ tetrahedra are generated, e.g., see Figure 21a.

- *Case-2 (edge-tri SSP):* The star-shaped polyhedron associated with a surface mesh point p, is constructed by deleting repeated edges/faces (tri/quad). In this case the cluster (ball) of the point p is comprised of triangles and tetrahedrons, deleting repeated interior edges/triangles in the ball of p, a star-shaped-polyhedron comprised of edges and/or triangles is constructed. After splitting point p, it is replaced by an edge $(p\bar{}q)$, and joining edges of the SSP to the edge $(p\bar{}q)$ generates tetrahedra, whereas joining triangular faces of the SSP to the edge $(p\bar{}q)$ in a consistent manner generates pyramids, as displayed in Figure 21b.

- *Case-3 (edge-tri-quad SSP):* In this case in the cluster (ball) of a point p, there exists pyramid(s) sharing point (p) to be split, e.g. see figure 21c. The star-shaped polyhedron associated with point p is constructed by deleting repeated interior edges, triangles and quads in the ball of p. The star-shaped-polyhedron constructed, is comprised of edges, triangles and/or quads. By splitting point p, an edge $(p\bar{}q)$ is obtained. By joining edge $(p\bar{}q)$ to each quad-face in a consistent manner a prism is constructed, e.g., see Figure 21c, whereas as mentioned above triangular faces yield pyramids and edges are used to construct tetrahedrons.

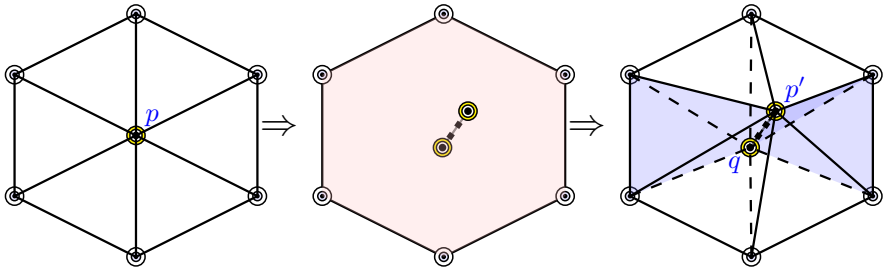

(a) Case 1: Cluster of p is comprised of triangles and star-shaped polyhedron reduces to a polygon, joining each edge of the polygon to edge (p', q) a tetra is generated

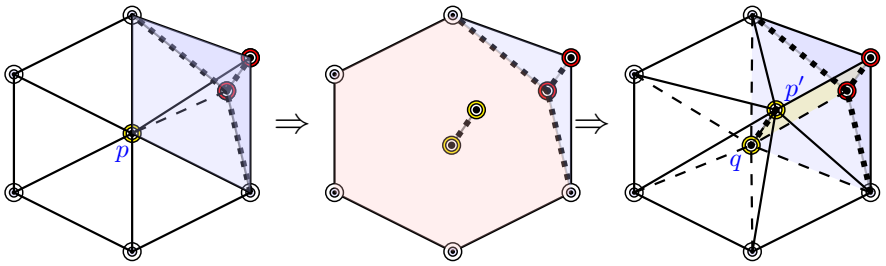

(b) Case 2: Cluster of p is comprised of triangles & tetras; joining each edge/tri of the star-shaped-polyhedron(SSP) to (p', q) a tetra/pyramid is generated

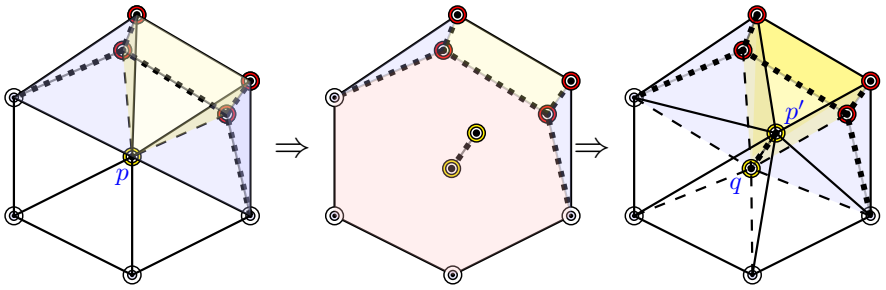

(c) Case 3: Cluster of p is comprised of triangles, tets and pyramids; in star-shaped polyhedron joining each edge/tri/quad to (p', q) a tetra/pyramid/prism is generated.

Figure 21: Procedure proposed for unstructured halo construction, operating on each mesh-point of the underlying surface, the halo enclosing the surface is constructed in an unstructured manner

D. Suppressing Steiner points (Special Case)

If suppressing a Steiner point to recover an underlying quad face as a set of two triangles, and the degree of the cluster (number of cells sharing the Steiner point at hand) is two, then it is checked against a special case. The special case occurs when connectivity of both cluster elements (tets) is defined by points constituting halo sub-faces (triangles) supported by the Steiner point being lifted. Figure 22a displays this special case, where to recover edge ac subdividing the underlying quad($abcd$) into two triangles($\triangle abc, \triangle cda$), a Steiner point($p$) was introduced and there are two tetrahedrons ($abdp, bcdp$) sharing the Steiner point(p). This case is simply dealt with by deleting the Steiner point(p) and updating the mesh locally, i.e., two tetrahedrons($abdp, bcdp$) sharing Steiner point(p), are replaced with a tetrahedron($abcd$) constituted by points defining a non-planar quad face, e.g., see Figure 22b.

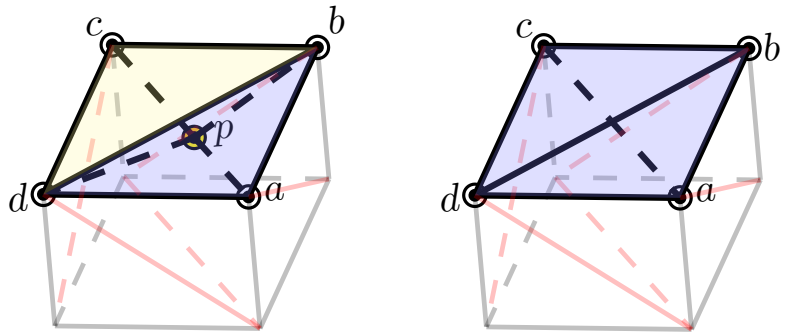

(a) Steiner point(p) is introduced to recover diagonal ac constituting halo quad ($abcd$)

(b) Delete Steiner point and replace two tetra sharing it, with one tetra defined by quad-face

Figure 22: Special case encounters when suppression of Steiner point, is performed by deleting the Steiner point

E. Constructing pyramid as transition element (Special Cases)

Special-Case 1 (combining two tets abutting a quad-face into a pyramid): In the case of a cluster of the edge, comprised of two tetra being removed, then such tets can be combined into a pyramid provided the point opposite to the underlying quad face is limited by a distance representative of spacing of points constituting the quad. Figure 23 displays an edge ac and two tetrahedrons $(abcp, acdp)$ sharing it. The point opposite to the quad face, i.e., p is used to construct a pyramid $(abcdp)$ abutting the halo, thereby replacing two existing tetrahedrons $(abcp, acdp)$.

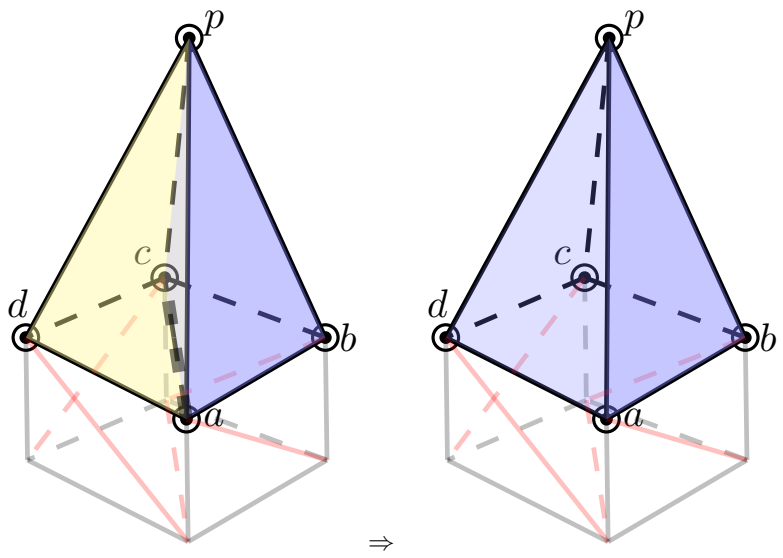

Figure 23: Special case encountered when constructing pyramid transition elements, used to recover underlying quad faces of the halo elements.

Special-Case2 (degree of edge-cluster is one): The construction of a star-shaped polyhedron from a set of elements sharing an edge (edge-cluster) bi-secting an underlying quad into two triangles, requires deleting interior faces. A special case is encountered when the degree of the edge-cluster is one. The degree of an edge-cluster being one, implies that there exists a tetra with its

connectivity defined by the point set constituting the quad face to be protected by constructing a pyramid. Figure 22b displays a case where a representative edge(ac) bisecting the halo quad ($abcd$) into two triangles ($\triangle abc, \triangle acd$) has one tetrahedron($abcd$) sharing it. This situation requires special treatment and we propose to construct a pyramid abutting a quad ($abcd$) by operating on the other possible diagonal of the underlying quad face, i.e., bd in Figure 22b. Note that the other possible diagonal of an underlying quad is an integral part of the tetra constituted by the quad-face and being inside the domain, is shared by more than one tetra. This switching of an edge bisecting an underlying quad face into two triangles consistently yields valid meshes, thereby protecting quad-faces by pyramids.